

USGS Award #G14AP00134

Paleoearthquake investigation of the Denali fault at the Nenana River, Alaska: Towards a 3000 year record of prehistoric earthquakes west of the 2002 rupture

Sean P. Bemis
Dept. of Earth & Environmental Sciences
University of Kentucky
101 Slone Research Building
Lexington, KY 40506

sean.bemis@uky.edu

Phone: (859)257-1374

Fax: (859)323-1938

Award Term: Sept. 1st, 2014 – Aug. 31st, 2015
(additional 1-year no-cost extension to Aug. 31st, 2016)

The Denali fault in south-central Alaska is a major right lateral strike-slip fault that parallels the Alaska Range for much of its length. This fault represents the largest seismogenic source for interior Alaska but due to its remote location and difficulty of access, a dearth of paleoearthquake information exists for this important feature. The fault system is over 1200 km in length and identification of paleoseismic sites that preserve more than 2-3 paleoearthquakes has proven challenging. In 2012 and 2015, we developed the 'Dead Mouse' site, which provides the first long paleoearthquake record west of the 2002 rupture extent. This site is located on the west-central segment of the Denali fault near the southernmost intersection of the Parks Highway and the Nenana River (63.45285, -148.80249). We hand-excavated three fault-perpendicular trenches and documented new evidence for six surface rupturing paleoearthquakes from deformation in the upper 2.5 m of stratigraphy. Evidence for these events include offset stratigraphy, filled fissures, upward fault terminations, and an angular unconformity. Radiocarbon constraints on earthquake timing are based upon OxCal sequence modeling, which reveals the following 2- σ age distributions; E1 to 440-316 cal yr BP, E2 to 835-740 cal yr BP, E3 to 1387-1126 cal yr BP, E4 to 3790-3020 cal yr BP, E5 to 5161-4531 cal yr BP and E6 to 7264-4943 cal yr BP.

1.1 Introduction

On the 3rd of November 2002, a M_w 7.9 earthquake sequence ruptured 341 km of the Denali fault (Figure 1) producing the largest strike-slip earthquake in North America in almost 150 years (Eberhart-Phillips et al., 2003). At the time this was the only known historic, or otherwise, surface rupturing earthquake on the Denali fault. This event initiated an increased interest in and highlighted the lack of knowledge concerning seismic hazards present in south-central Alaska. Following the 2002 earthquake, the Denali fault has been a primary target of paleoseismic investigations and represents the largest seismogenic source for interior Alaska (Wesson et al., 2007). Results from investigations along the Denali fault system have revealed anywhere from 1 to 5 paleoearthquakes at 17 different sites, 14 of which only document evidence for 3 or fewer earthquakes (Figure 1; Koehler et al., 2011; Personius et al., 2015; Plafker et al., 2006; Schwartz et al., 2005, 2012, and 2014; Seitz et al., 2008). During the summers of 2012 and 2015, we developed a new paleoseismic site, ‘the Dead Mouse site’, located on the west-central segment of the Denali fault near the southernmost intersection of the George Parks Highway and the Nenana River (63.45285, -148.80249) (Figure 1). The Dead Mouse site is located ~70 km from the western end of the 2002 Denali fault earthquake sequence (DFES) surface rupture terminus and ~40 km west of the M_w 6.7 Nenana Mountain foreshock epicenter. The site is the most accessible paleoseismic site on the entire Denali fault system, as it is situated about 400 m from the highway (800 m by trail) and provides the only paleoseismic study directly within the Parks Highway infrastructural corridor.

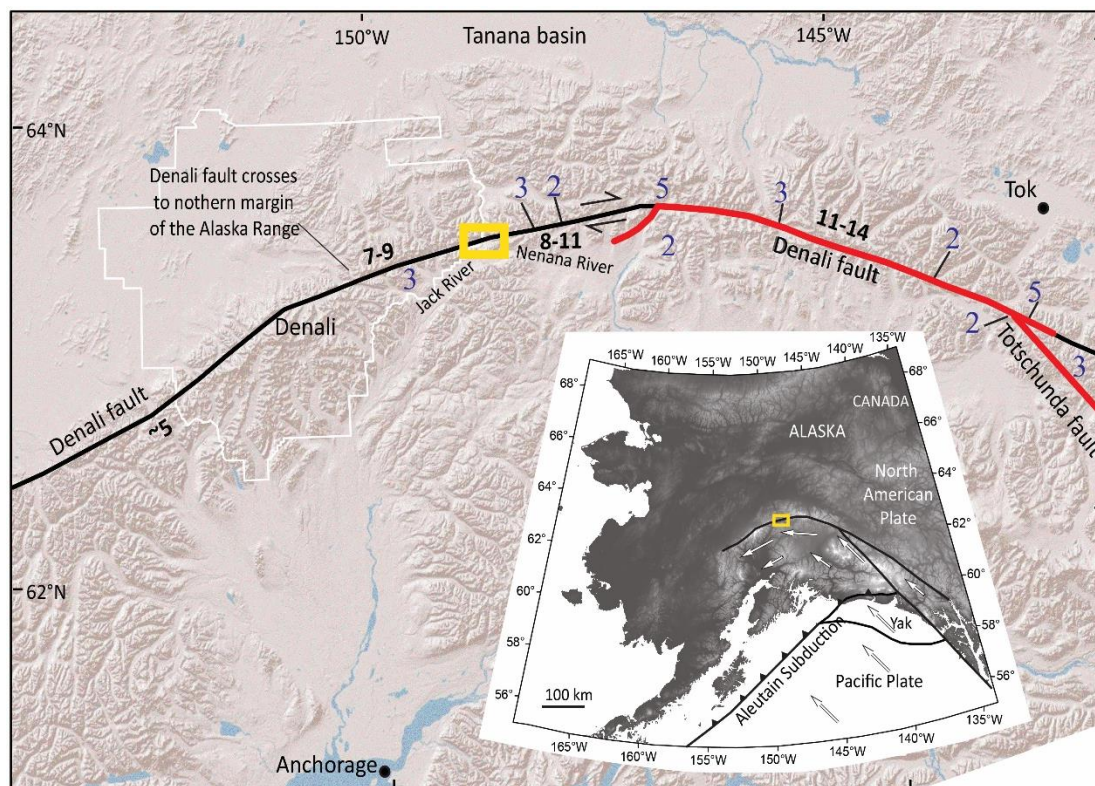


Figure 1. Regional topography, geographic features and orogen-scale structures of the Alaska Range-Denali fault system. White outline delineates the boundary of Denali National Park and Preserve. Black numbers are late Quaternary slip rates (mm/yr) generalized from Matmon et al.

(2006), Meriaux *et al.* (2009), and Haeussler *et al.* (2012). The inset map depicts the major active tectonic elements for south-central Alaska with arrows depicting plate motions relative to stable North America (modified from Freymueller *et al.*, 2008). Yak is the unsubducted portion of the Yakutat microplate. The red line approximates the November 3rd 2002 M7.9 rupture extent. The yellow boxes outline the location of the Dead Mouse site and Figure 2. Blue numbers represent paleoseismic sites with number of events recorded (Koehler *et al.*, 2011; Personius *et al.*, 2015; Plafker *et al.*, 2006; Schwartz *et al.*, 2005, 2012, 2014 and in review; Seitz *et al.*, 2008).

The Denali fault is a major right-lateral intracontinental crustal strike-slip fault that closely parallels the Alaska Range as it spans much of south-central Alaska from east to west (Figure 1). The fault and the elevated topography of the Alaska Range occur as far-field deformation from the collision and oblique flat-slab subduction of the Yakutat Block along the Pacific-North America plate boundary in southern Alaska (Eberhart-Phillips *et al.*, 2006; Haeussler, 2008). This far-field deformation extends into the interior of south-central Alaska and is accommodated through dextral slip on the Denali fault system (Bemis *et al.*, 2015, Haeussler, 2008). Dextral displacement initially developed along what is understood to be a structurally weak suture zone (e.g. Ridgway *et al.*, 2002) and has a post-Cretaceous dextral displacement west of Denali estimated to be approximately 140 km (Miller *et al.*, 2002) and late Cretaceous to early Tertiary displacement of about 400 km on the eastern section of the fault (Grantz, 1966; Nokleberg *et al.*, 1985; Hickman *et al.*, 1990; Plafker and Berg, 1994). Additionally, the Denali fault has the greatest slip rate of all non-plate boundary active faults for Alaska. Late Quaternary slip rates range from ~7 to 14 mm/yr with a clear pattern of westward-decrease in velocity, west of the Totschunda fault intersection (Matmon *et al.*, 2006, Meriaux *et al.*, 2009, and Haeussler *et al.*, 2012) (Figure 1).

In 2012, we identified a narrow zone of fault scarp morphology expressed as localized pull-apart depressions and left-stepping *en echelon* shears on a set of abandoned fluvial terraces near the eastern margin of the broad floodplain of the Nenana and Jack Rivers (Figures 2 and 3). Initial site reconnaissance and soil auger examinations revealed 1-3 m of bedded fine-grained silt, sand and organic-rich horizons. During the summer months of 2012 and 2015 we hand excavated three fault-perpendicular trenches across portions of the fault scarp on the lowest terrace (Figure 4). Trenching revealed evidence for up to six events in the upper 2.5 m of stratigraphy that spans ~6,000 years. We infer five events from primary evidence directly correlating with surface rupture and one additional event on the basis of secondary structural evidence. Evidence for these events include offset units, filled fissures, upward fault terminations, angular unconformities and broad zones of multiple lines of evidence within primary fault zones, as well as distributed deformation, are apparent for each event in all three trenches. Radiocarbon samples and modeling constrain the six events to the following 2- σ age distributions; E1 to 440-316 cal yr BP, E2 to 835-740 cal yr BP, E3 to 1387-1126 cal yr BP, E4 to 3790-3020 cal yr BP, E5 to 5161-4531 cal yr BP and E6 to 7264-4943 cal yr BP. We have developed the new Dead Mouse site by: 1) producing orthorectified photomosaics used for hand-mapping structural evidence and stratigraphy, 2) constructing a georeferenced 3D site model to better constrain structural interpretations and stratigraphic correlations, 3) processing 49 radiocarbon geochronology samples that include leaves, seeds, woody macrofossils, and detrital and in-situ charcoal; and 4) developing an event chronology through the integration of relative

ages, calibrated radiocarbon sample ages and one tephra age through OxCal sequence modeling (Bronk Ramsey, 2008; 2009a)

This study presents a descriptive characterization of the Denali fault at the confluence of the Nenana and Jack rivers, a classification of stratigraphic units west of and adjacent to the active floodplain, a synthesis of prehistorical earthquake evidence, and chronological modeling of paleoevent timing based upon calibrated radiocarbon ages and sequence modeling. The Dead Mouse site provides the first long paleoearthquake record west of the 2002 DFES rupture terminus, constraining event timing for the past ~6000 years. The evidence for six events and their respective timing provides the opportunity to discuss along-fault paleoearthquake correlations, it improves prehistorical event history completeness, constrains estimated slip-per-event parameters, and provide a better understanding of earthquake behavior, providing critical details for future hazard mitigation.

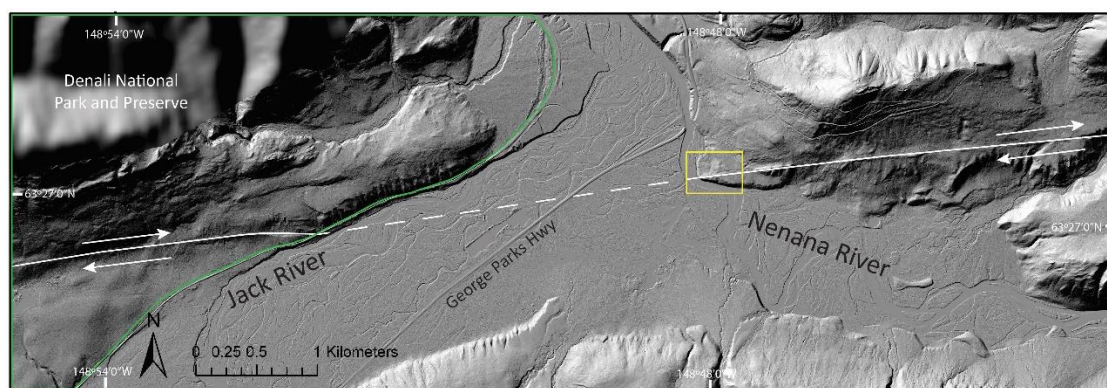


Figure 2. Site location map at the confluence of the Jack and Nenana Rivers, east of the George Parks highway. Yellow box outlines Dead Mouse site. White lines represent geomorphic expression of Denali fault. Denali National Park and Preserve boundary, west of the Jack River, is shown with a green line.

1.2 The Denali fault at the Nenana River

Quaternary glacial advances intermittently covered most of southern Alaska and the Alaska Range, with interior Alaska remaining largely unglaciated (e.g., Hamilton, 1994; Briner and Kaufman, 2008). Ice repeatedly accumulated along the axis of the Alaska Range throughout the Pleistocene, flowing to the north as lobes through the Alaska Range foothills and coalescing to the south as large ice streams. Modern glaciers emanate from the higher elevation regions of the Alaska Range. The Nenana River has its source in the Nenana Glacier on the south side of the Alaska Range, it traverses the south flank of the range for ~50 km, turns north and flows through a saddle in the axis of the Alaska Range. This river appears to have entrenched itself in the current course following deglaciation of this region at ~16 ka (Dortch et al., 2010), although northward sediment transport across this portion of the Alaska Range has occurred for several million years (e.g., Thoms, 2000; Ridgway et al., 2007).

Our initial efforts at the Dead Mouse site were directed at attempting to find potential lacustrine deposits within the Nenana River floodplain as a possible product of a hypothetical landslide-dammed lake. Keskinen and Beget (2005) recognized a large landslide deposit ~4 km north of the Dead Mouse site and suggest it may have been triggered by the most recent event on

the Denali fault 300-500 years ago. Newly available airborne lidar data from the Alaska Division of Geological & Geophysical Surveys (Hubbard et al., 2011) captures the landslide morphology and the Denali fault scarp morphology where the fault intersects the Nenana and Jack Rivers. In these data, the Denali fault has a clear geomorphic scarp across the landscape where surface morphology is not fluvially reworked in active river floodplains or actively occupied glacial valleys. Our initial focus proved unsuccessful and we redirected our efforts toward investigating locations for developing a new paleoseismic site. We used a soil auger to examine the deposits along the Denali fault scarp east of the Nenana River, where we discovered a significant thickness of fluvial sand and silt above a gravelly terrace tread. Additionally, vertical offsets of the gravelly terrace tread were obvious between adjacent soil auger holes. Following the discovery of the vertical offsets and fine-sediments with minimal permafrost we began developing the new 'Dead Mouse' paleoseismic site.

Previous regional-scale geologic mapping near the Dead Mouse site does not differentiate Quaternary deposits (Sherwood and Craddock, 1979; Csejtey et al, 1992). Our work revealed that these were well-sorted, well-rounded sediments most indicative of fluvial and/or aeolian input. The terrace tread is comprised of well-rounded medium-grained granodiorite gravel to boulders.

The fault scarp at the Dead Mouse site consists of several left-stepping, west-northwest trending *en echelon* fissure-like landforms across the trend of the long-term geomorphic scarp (Figure 3). The minimal degradation of these geomorphic scarp features provided compelling evidence that structural evidence for recent earthquakes would be preserved in the subsurface, and soil-auger transects demonstrated the presence of layered fine-grained sediment. We located the trenches across these fissure-like features and, in particular, where soil-auger transects identified offsets in the surface of the terrace gravel (Figures 3 and 4). Initial reconnaissance established the limited geographical extent for hand-excavation trenching, site development and expansion. The only recognized location that allowed hand-excavation at the site is restricted to about 20 m of the fault trace between the crest of the lowermost terrace riser and the onset of permafrost eastward along the fault (Figure 4).

During summer 2012, we hand-excavated two trenches at the Dead Mouse site and then returned in 2015 to re-excavate and extend the Dead Mouse trench 1 (DM1) to the north (Figures 5 and 6). The length of our extension was limited by the locations of large white spruce (*Picea glauca*) trees and thick vegetation; therefore, we stepped the DM1 excavation to the east and continued north until vegetation again restricted a northward advance (Figure 5). At this point, we hand-excavated a third trench (DM3), to the east and parallel to the extended portion of DM1 (Figures 4 and 5). Trench three overlaps the northern margin of trench one by ~2 m and exposed an additional ~1 m north along the same trend, perpendicular to the geomorphic fault expression.

Our trenches exposed 1-2.5 m of fine-grained sediments above a gravel contact, and fluvial sediments interbedded with buried soils and organic-rich horizons preserving distinct cross-cutting relationships between offset stratigraphy and overlapping undeformed strata (Figure 7). Furthermore, trenching revealed that deformation is distributed over a zone of ~12 m such that, in our exposures, individual earthquakes produced multiple displacements and older events were preserved in stratigraphy undeformed by subsequent events (Figures 9 through 14).

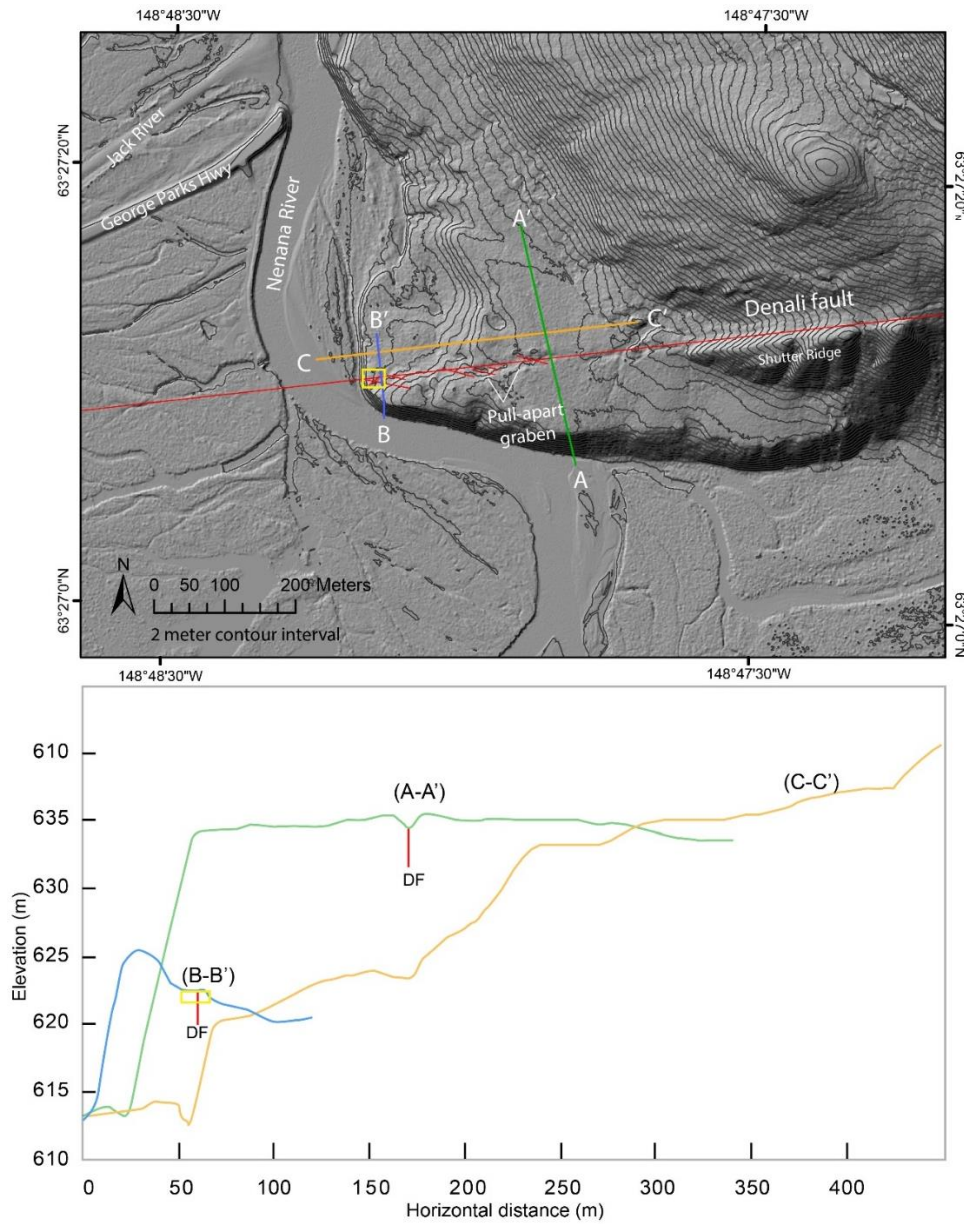


Figure 3. Lidar derived digital elevation model with 2 m contour intervals. Red lines highlight the main trace of the Denali fault and left-stepping en echelon shears. Elevation profiles in green, blue and orange. These profiles highlight the lack of long-term vertical displacement with nearly planar terrace tread morphology. Yellow boxes outline the Dead Mouse site.

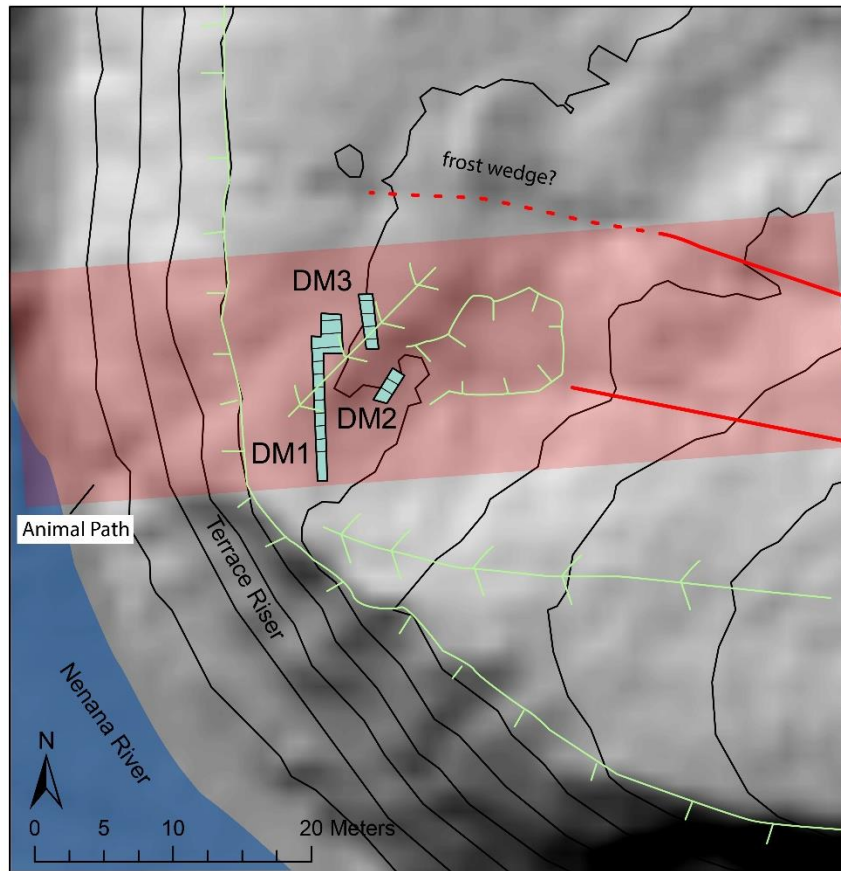


Figure 4. Half-meter resolution lidar with 2 m contour intervals. Dead Mouse trench locations. Light green lines map geomorphology, tick marks indicate topographic relief. Solid red lines are en-echelon surface ruptures. Dotted red line is linear topographic low interpreted as frost wedge or extension of animal trail. Opaque red polygon shows the main trend of the Denali fault at the site and the width of surface deformation.



Figure 5. A) Dead Mouse site view to the north B) Dead Mouse site view to the northwest of trench 1 extension and trench 3. DM– Dead Mouse. Note the black spruce trees impeding continual excavation to the north. Yellow- trench 1, pink- trench 2, blue- trench 3.



Figure 6. Dead Mouse trench one extension exposed interbedded sands, silts and organic-rich horizons. View to the northeast. East wall exposure with deformation relating to event 2. Fault zone seen on east wall was similarly expressed on trench floor and traced into southwest corner of the west wall.

2. Methods

2.1 Paleoseismic Investigation

Trenching

During the summer field seasons of 2012 and 2015 we hand-excavated three fault-perpendicular trenches following protocols described by McCalpin (2009). We excavated trench one, the longest of the three, nearest to the western margin of the lowermost tread (Figure 4). This area provided the greatest opportunity for one long continuous trench, perpendicular to the main fault trend with limited vegetation. Trench one trends north to south and spans ~12 m long and 1 m wide with a slight jog to the east and extending to the north on the north side of the trench. We excavated trench two ~2 m east of trench one across a surface depression that we interpret as an *en echelon* shear from the lidar data (Figure 4). Trench two trends northeast to southwest and is 3.25 m long and 1 m wide. Trench three is located east of trench one and north of trench two (Figure 4). It was excavated to continue our northward progression through the fault zone. The southern two meters of trench three overlap the northern two meters of the trench one extension and provides an additional meter of exposure to the north. Trench three is 3.5 m long and 1 m wide. Each of these trenches provided cross-sectional exposures of generally fine-grained fluvial sediments and coseismic deformation. Trench depth was constrained by the presence of fluvial gravels, cobbles, and boulders. After excavating trench one and trench three,

we used a frost probe (a thin, pointed, hardened steel 1.5 m long rod that is pushed into fine-grained sediments to detect the depth to frozen ground or coarser sediments) to record depth from trench floor to gravel contact. We probed down the center of trench one and trench three at half meter spacing (Figures 9, 10 and 13).

Following trench excavation, we mapped and documented the trench walls with regards to lithologic and pedological differences in size, shape, sorting, color and recorded primary and secondary evidence for active faulting. We conducted our mapping on high-resolution orthorectified photomosaics produced with Agisoft Photoscan Pro, following a similar process to that described in Bemis et al. (2014) and Reitman et al. (2015). We printed orthomosaics for each of the trench walls at a 1:5 scale and used these printouts as a base map to record fine-scale details.

We used hand held Trimble differential GPS and a Trimble robotic total station to perform a field survey of trench boundaries, grid nodes, frost probe transects and other points of interest. Our survey was performed by establishing a diamond shaped perimeter of four control points that spanned the entire site. These four control points became our references for setting up the total station at different locations providing clear line of sight to points of interest. Additionally, the perimeter of control points established reference points to maintain internal consistency. We surveyed each of our features in a local coordinate system that resulted in sub-centimeter internal accuracy. After surveying we recorded control point locations with the GPS at decimeter-scale precision. Upon returning to the lab, we integrated the survey data with measured coordinates of control points and spatially adjusted the survey data.

2.2 Dating

Radiocarbon Dating

The stratigraphy at the Dead Mouse site contains multiple distinct organic horizons, as well as local disseminated organic fragments. The clear stratigraphic differences and abundance of organic matter provide the framework for our chronological modeling. We collected samples of wood fragments, leaves, seeds, in-situ charcoal and detrital charcoal from distinct stratigraphic horizons. Our sample selection processes focused on obtaining a distribution covering each identifiable horizon to capture the full vertical extent from each of the trenches. Additionally, we focused our efforts on obtaining samples that most closely bracketed paleo-event horizons. Each of the samples were packaged in glass vials or wrapped in tinfoil in the field. Upon returning to the University of Kentucky radiocarbon lab we dried samples in a low air temperature oven and those selected for radiocarbon analysis were examined under a binocular microscope to record sample type and quality. To prevent contamination, samples were handled with tools cleaned with denatured alcohol. Prior to accelerator mass spectrometry (AMS) analysis, we removed modern root hairs and other macroscopic contaminants from samples by hand. We handpicked specific organic fractions (e.g., detrital charcoal, seeds, twigs, etc.) from samples that consisted of fine-grained disseminated organic material to reduce potential uncertainty from amalgamating sample material with different ages. We prepared 49 samples from a distribution spanning three trenches and 23 different stratigraphic units. After samples were prepared we sent them to be processed by AMS.

3. Results

3.1 Stratigraphy

Sediments at the Dead Mouse site consist of ~2-2.5 m of layered sand, silts and organic dominated horizons deposited over fluvial sands, gravels, cobbles and boulders (Figure 7). The source of the fine-grained sediments is an intriguing aspect of this site. The modern terrace surface at the trench site is ~8 m above the modern Nenana River, and 4-6 m higher than the broad floodplain surface at the confluence of the Nenana and Jack Rivers (Figures 3 and 4). Located within Windy Pass and proximal to a glacially-sourced river, some of the silt in the stratigraphic section is likely aeolian, having been mobilized from the adjacent active floodplain. However, much of the stratigraphy is moderately well-sorted, mm to cm-scale bedded, medium and coarse sand that suggests a fluvial origin (Figure 7). Each of the three trench exposures reveal tabular packages that are laterally continuous, yet exhibit variability in grain-size, thickness, color, sorting and organic content. Broadly, the fluvial units thicken and dip westward toward the terrace riser with the active floodplain. However, horizon thicknesses also closely correlate with vertical patterns of slip in each earthquake. The greatest vertical unit thicknesses are observed directly above filled fissures and other zones of localized depression from tectonic deformation. The lower meter consists of three fining upward sequences. These three sequences are relatively similar and consist of a basal yellow-gray medium-grained well-sorted sand, fine upward and are capped by a dark-brown to purple organic-rich silt horizon. The basal sands vary greatly with lateral continuity (Figure 7). The uppermost meter of stratigraphy is comprised of a fiber-dominated modern organic-rich horizon, multiple massive silt horizons, bedded silt and bedded sand horizons (Figure 7). Few sections have clear continuity whereas others have a wavy discontinuous fabric. Nearly all of the basal sands have scour and fill structures, likely representing erosional gaps in sedimentation at the U60/U70, U70/U75 and U81/U90 contacts (Figure 7). Lower in the section, a light-tan tephra is present in each of the trenches.

We classify and subdivide most sedimentary packages into lithologic units based on color, grain size, texture, sorting, and bedding (Figure 7). Additionally, we identify multiple organic-rich soil horizons (Figure 7). Our classification consists of primary and secondary units. Primary units are assigned a unit identity based on multiples of 10. Increasing unit number corresponds with an increase in relative age and depth from the surface. Subunits are differentiated by numbers between multiples of 10 (i.e. 31, 32, 33...). These subunits also increase numerically with relative age. In general, subunits identify lateral sedimentological change (i.e., areas of additional sedimentation) or inconsistencies with the framework of unit packages; that were established on different trench walls. We subdivide the stratigraphy into 23 units and subunits. We have identified five event horizons where overlying undeformed units are in contact with underlying deformed units. Identifiable event horizons include, U30, U41, U51, U75 and U110 (Figure 7). Additionally, event indicators inferred from a soil probe and the unit exposures on DM3 suggest an event horizon is located between U75 and U100 immediately below the floor of DM1 (Figure 9). Although U40 and U41 are lithologically indistinguishable, the contact is based upon the juxtaposition of overlying horizontally undisturbed sedimentation in contact with lower deformed and disrupted textures of seismogenic origin. Also, subunit U51 represents a recognizable expansion of U50 where multiple thin organic horizons are individually distinguishable (Figure 8). Units U50 and U51 have lateral variability in unit thickness. These units appear to represent multiple pulses of organic development contemporaneous with variable lateral deposition of silt. The contact between these two units represents organic development that predate and postdate a prehistoric earthquake.

Subunits U71-U74 are only recognizable on the west wall of trench one. The subunits are part of a synclinal fold that was subsequently cross-cut by an angular unconformity (Figure 9). On the southern limb of the fold this angular unconformity cross-cuts U71, U72, U73, U74, U75 and U80 (Figure 9). To the north, U71-U74 are cross cut but the unconformable contact continues to the north between U70 and U75. This contact represents a significant temporal gap in sedimentation.

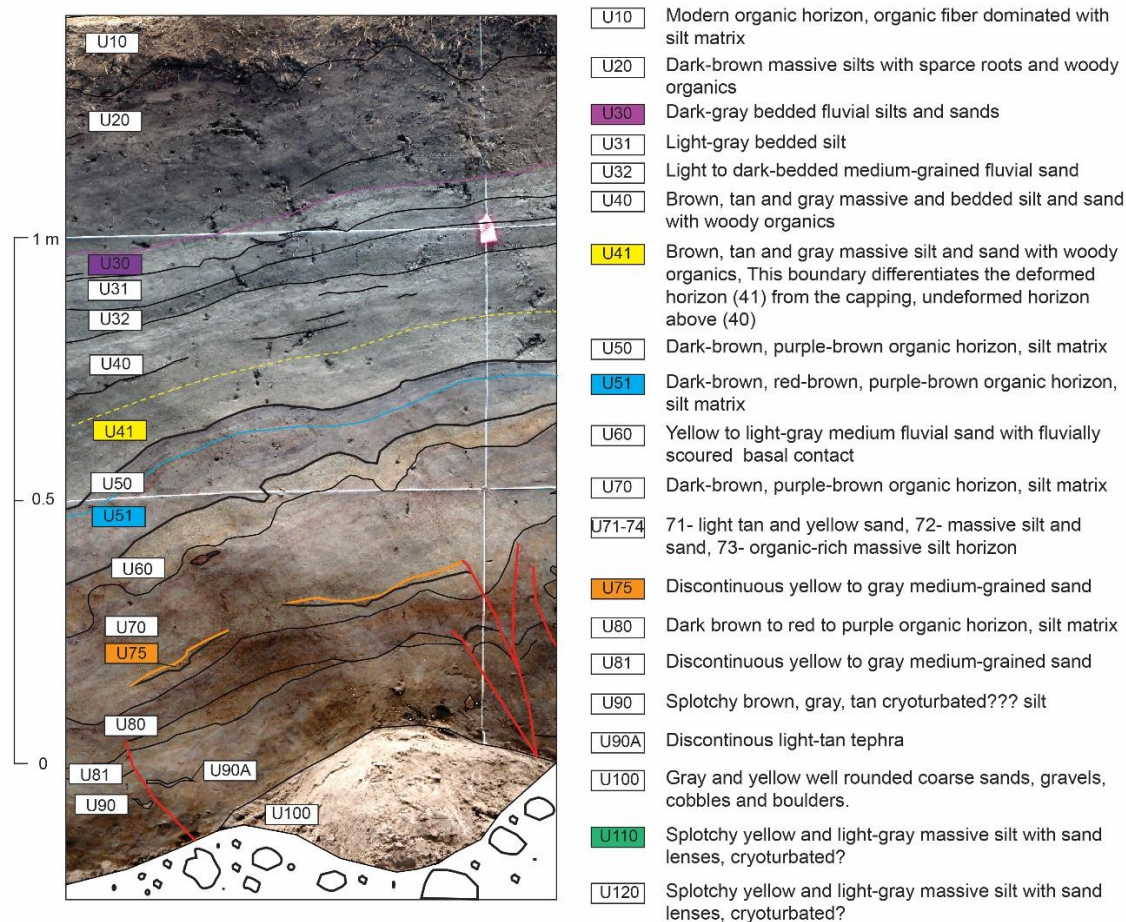


Figure 7. Generalized stratigraphic column at the Dead Mouse site. Unit descriptions, names and subdivisions. Colored lines indicate event horizons. Purple- Event 1, Yellow- Event 2, Blue- Event 3, Orange- Event 4 and green box- Event 6. Precise location of the Event 5 horizon is unknown, however it can be constrained to below U81 and above the top of the U100 fluvial gravel contact (Figures 9 and 10)

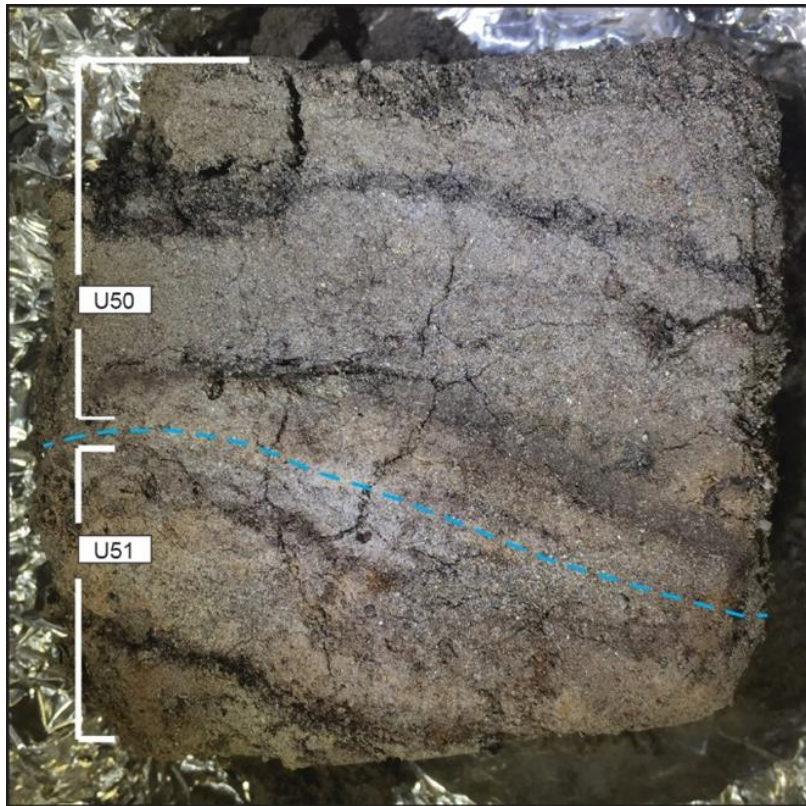


Figure 8. Example of unit 50 and 51 from east wall of trench one at meter 4.7(Figure 10). Unit 50 is largely a homogeneous organic-rich silt, but locally the unit thickens and is characterized by discrete organic horizons separated by additional silt deposition. We infer that this develops through differential sedimentation from topographic variations, wherein low topographic relief receives greater deposition and a thickened stratigraphic section. These thickened sections of stratigraphy make it possible to identify multiple soil developments that span about 300-400 years, and results in improved age constraints for Event 3.

3.2 Event Evidence

The geomorphic evidence for the Denali fault scarp at the Dead Mouse site is expressed as a semi-irregular pattern of narrow, linear topographic troughs and hummocks on terrace tread surfaces that post-date the last glacial occupation of the valley at ~16 ka (Dortch et al., 2010) (Figures 2 through 4). The 2002 DFES provides the only direct example of geomorphologic fault expression from historical rupturing events on the Denali fault. From this event, Eberhart-Phillips et al. (2003) and Haeussler (2009) observed offset features, extensional and contractional stepovers, *en echelon* fissures, and Riedel shears in snow, glacial ice, and sediment. According to their observations, overall vertical-slip was minimal, whereas dextral displacements comprised the majority of the observable features (Eberhart-Phillips et al., 2003; Haeussler, 2009). Others have observed nearly continuous surface ruptures with left-stepping surface tears and average DFES lateral offsets of 4.5-5.1 m and 5-8 m (Haeussler et al., 2004; Schwartz et al., 2003). These studies provide characteristic surface expressions and rupture patterning that enable better interpretation of paleo-event evidence.

Although studies of the 2002 DFES were able to determine characteristic faulting parameters and structural constraints along the surface rupture, prior to this event little was known about large ($>M_w 6$) prehistoric surface rupturing events in terms of temporal and geographical distribution. Therefore, following the 2002 event there was a USGS-led multi-year effort to develop new paleoseismic sites, resulting in the development of 17 new paleoseismic sites. Results from these investigations along the Denali fault system, document one to five paleoearthquakes at 17 different sites, 14 of which only document evidence for three or fewer earthquakes (Koehler et al., 2011; Personius et al., 2015; Plafker et al., 2006; Schwartz et al., 2005, 2012, and 2014; Seitz et al., 2008). Evidence for faulting from distinct events at these sites includes upward fault terminations, scarp-derived colluvial wedges, filled fissures, folding, shutter ridges, sag ponds, tectonic pushups, *en echelon* left and right stepping fault strands, buried trees, damaged trees, and soft-sediment deformation related to shaking and liquefaction (Koehler et al., 2011; Personius et al., 2015; Plafker et al., 2006; Schwartz et al., 2005, 2012, and 2014; Seitz et al., 2008). Schwartz and others (2005) reported evidence for 2-3 events ~40 km west of the Dead Mouse site, within the Denali National Park and Preserve. Personius and others (2015) document three events and infer a fourth, most recent event, on the basis of fresh geomorphic expression of the fault scarp at the Schist Creek site, ~19 km east of the Dead Mouse site.

Although degraded by erosion and overgrowth, the Dead Mouse site exhibits many similar characteristics as the 2002 Denali fault surface rupture (e.g. Haeussler, 2004). The Denali fault strikes east to west across the Dead Mouse site and is expressed with a series of left-stepping *en echelon*, decimeter-scale linear surface depression that we infer formed from rupture fissures. Additional surficial features preserved along the fault scarp include shutter ridges, pressure ridges, and small pull-apart grabens (Figure 3). East of the Dead Mouse site, the Denali fault crosses an older, likely early Holocene fluvial terrace (Figure 3). A fault-perpendicular elevation profile extracted from 0.5 m resolution airborne lidar data along this terrace exhibits no appreciable long-term vertical offset across the fault at this site (Figure 3). The surficial evidence of Holocene fault displacement is constrained to a narrow zone of trough-like landforms (fissures and small pull-aparts) providing the opportunity to minimize workload of hand-trenching efforts to span the full width of fault deformation.

Our paleoseismic trenching at the Dead Mouse site documents multiple lines of primary evidence for five surface rupturing events and structural evidence for one additional event. We summarize evidence for each of the six events based on evidence type, location, and relative timing (Table 1). The evidence used to define these earthquakes includes filled fissures, vertical offsets, upward fault terminations and truncations, horizontal shortening, lateral thickness changes, an angular unconformity, and distributed zones deformation. In total, we have identified five event horizons including U30, U41, U51, U75, and U100. A sixth event is inferred from subsurface evidence obtained by inserting a frost probe into the floor of DM1 and recording depth to the U100 contact. We can constrain this event stratigraphically as older than the U81 contact and younger than U100.

3.2.1 Event 1

Evidence for event one (E1; the most recent earthquake recorded at this site) was documented at two locations where deformation occurred above U40. Between meters 3-4 on the west wall in trench two exposed faults offset and cross-cutting older deformation at depth then

penetrate up through U30 as a discrete fault (Figure 12). Units U30 through U50 are folded and attenuated across the tip of this fault. The E1 event horizon U20, overlies the folding, increasing in unit thickness across the fold. This thickening suggests post-event deposition into a trough created by the surface deformation of E1 (Figure 12). The east wall of trench two, however, shows no deformation above U40 and demonstrates deformation for this event is highly-localized. Between meters 5 and 6, on the east wall of trench one, U30-U32 are also folded (Figure 10). However, no shear surfaces were identified below these folds and folding is not present on the west wall of the same trench (Figures 9 and 10). While the evidence for E1 is not as strong in trench one, we are confident in the event interpretation because of the correlated deformation of the same units from the east wall of trench one and the west wall of trench two. The folding in DM1 is in contact with large dead tree roots (Figure 10) and our preferred interpretation is that units U30-32 were folded as the tree collapsed in response to an earthquake. The subtleness of evidence and lack of broadly distributed evidence suggests this may represent an event with small surface displacement at the site.

3.2.2 Event 2

Evidence for event two (E2) is more distinct than E1 and it is present in each of the three trenches. Units 41 and 50 are cut by an oblique slip fault thrusting units to the NNW and are capped by U40 (F2a-b; Figures 9, 10, and 14). The thrust fault tip is located at meter 6 on the east wall and 5.5 on the west wall with. This fault has a strike of 050° , which is $\sim 037^{\circ}$ oblique to the Denali fault strike, leading to a localized zone of contraction (Figures 8 and 9). Slight surface uplift is evident in the lidar directly above meters 5-6 of trench one and correlates to the subsurface location of thrusting (Figure 5). Evidence for E2 also occurs on both walls of the trench one extension (F2c-d; Figures 10 and 14) and the E2 fault zone was traceable across the trench floor. The fault zone on the trench floor had a similar expression to the east wall with a texture displaying distributed deformation and bounded by planar faults. The E2 fault zone juxtaposes different unit thicknesses implying significant lateral displacement and terminates within U41 (F2e; Figures 12 and 14). Moreover, a small fissure (F2f) located at meter 0 on the east wall of trench three breaks up to U50 and is filled with U40 (Figures 13 and 14). Unit 50 also has evidence for faulting on the west wall of trench three, however the evidence is highly ambiguous due to the many roots and high degree of bioturbation (F2g; Figures 13 and 14).

3.2.3 Event 3

Units U31, U32, U33, U40 and U50 dip toward two filled fissures located between meters 0-2 of DM1 (Figures 9 and 10). These fissures offer the best evidence for Event 3 (E3: F3a-b and F3d-e; Figures 9, 10, and 14). They are bounded by linear fault traces and based upon their position on opposite trench walls, are oriented nearly parallel to the main trend of the Denali fault. Both of these fissures at the four cross-sectional exposures are bounded by faults, filled with sediments from fissure wall collapse and are capped by U50, a thin organic horizon. Units U50 and U51 vary laterally in thickness due to deposition, and multiple locations exhibit zones of expanded sedimentation (Figure 8). Otherwise, the majority of these two units merge into one organic-rich homogenous unit. Although U50 and U51 merge, E3 clearly faults the lower half of these amalgamated units and is subsequently capped by a thin organic-rich horizon (U50; Figures 9 and 10). Therefore, we interpret the event horizon to be U51 and the capping unit to be U50. Additional corroborating evidence for E3 includes an upward fault termination at the U50/51 boundary on the east wall of the trench one extension near meter 10 (F3c; Figures 11

and 14). This location shows a clear juxtaposition of units bounded by a curved fault trace and a thin tephra with ~0.5 m of vertical offset (F3c; Figure 11).

3.2.4 Event 4

We interpret event four (E4) based on the aggregation of features within zones of distributed deformation that spans 0.5-1 m on multiple trench walls (F4a-i; Figures 9-12 and 14) and the presence of an angular unconformity (Figure 9). These features include upward terminating faults, minor vertical offsets, minor fissures, horizontal shortening, unit thickness changes, folds, and an angular unconformity. The angular unconformity cross-cuts units 71-80. Units 71-74 are only recognizable on the west wall of trench one in the synclinal fold between meters 5-7 (F4f; Figures 9 and 14). Due to the isolated preservation of these units and their combined thickness of 25 cm, they represent a significant erosional gap in preserved history. The angular unconformity, as well as E4 upward terminations, are capped by a massive silt horizon (U70) with a soil development at the top of the unit. Multiple subtle upward fault terminations are distributed adjacent to folding of U75, as well as a horizontally shortened, vertically thickened U90A (F4a-b; Figures 10, 11, and 14). Excluding the angular conformity, individual pieces of evidence for E4 are significantly weaker than those identified for E2 and E3. However, when considered collectively, it is clear that these pieces of evidence correlate and support the identification of E4.

3.2.5 Event 5

Our interpretation of this event is based on a >1 m vertical offset in the fluvial gravels between meters 6 and 8 of trench one (F5a; Figures 9 and 10). We used a frost probe to record the top of the gravel contact and were able to identify the offset by inserting the full length of the probe (1.5 m) without contacting the fluvial gravel. This vertical offset is not represented in the overlying exposed stratigraphy. Structurally the overlying sediments are sub-horizontal and folded fine-grained beds that appear to generally dip to the north but are highly disrupted due to tectonic deformation or cryoturbation. Additionally, the lower stratigraphic section (U90?) appears to be truncated by the fluvial gravels (U100?). Stratigraphically, this event can be constrained to below U81 and above the top of the U100 fluvial gravel contact.

3.2.6 Event 6

Event six is the oldest and evidence for this event is only expressed at one location on the east wall of trench three (F6a; Figures 13 and 14). The event evidence includes upward fault terminations and vertical offsets that form a horst and graben-type structure (F6a; Figures 13 and 14). The faults and structural evidence are distributed over 75 cm and are capped by reworked rounded sand to boulder-sized matrix supported sediment. Multiple fault strands are capped by U100, however, it appears that the gravel was subsequently faulted by a younger event. Structural evidence of the faulted overlying gravel unit does not correlate with the underlying preserved structure of E6. In particular, the horst-type vertically offset upward structure is directly below a downward vertical offset of the overlying gravel unit (Figure 13). In addition to structural differences, a disconformable contact occurs between U100 and U120. It appears that U110 of the raised horst was eroded then capped by U100 during a high-energy depositional episode. This erosional contact suggests that the faults have been crosscut by erosion and their upward termination has the greatest potential for chronological uncertainties.

Table 1. List of event evidence at the Dead Mouse site.

Dead Mouse Event	Wall	Event Evidence	Event Horizon	Capping Horizon	Meter	Fault Label	Description and Interpretation of event evidence
E1	DM1EW	Fold	30	20	4-6		Folded well-bedded fine to coarse sand. Correlates with localized surface uplift
E2	DM1EW	vo	U41	U40	6	F2a	Thrust fault plane appears to be a right-stepping oblique fault with localized contraction.
E2	DM1W W	vo	U41	U40	5.5	F2b	Thrust fault plane appears to be a right-stepping oblique fault with localized contraction.
E2	DM1EW ext	utf, fis, vo	U41	U40	9-9.5	F2c, F2d	Broad fault zone deformation.
E2	DM1W Wext	utf, fis	U41	U40	9.5-10		Units dip into fault zone, Majority of evidence removed during excavation. However, faulted zone is clearly expressed on trench floor and intersects southern corner of the west wall.

Table 1. (Continued)

E2	DM2WW	utf	U41?	U40	0.5	F2e,	E2
E2	DM3EW	utf, fis	U41?	U40	0, 2.75	F2f, F2g	Minor faulting yet apparent fissure filled with U40
E2	DM3WW	?	?	?	?		There appears to be faulting that faults U50 but this wall is very difficult to interpret due to the many roots and bioturbation/cryoturbation
E3	DM1EW	utf, fis	U51	U50	0-1.75	F3a, F3b	Filled fissures, oriented parallel to main fault trend.
E3	DM1EWext	utf, vo	U51	U50	10	F3c	Tephra vertical offset ~0.5 m
E3	DM1WW	utf, fis	U51	U50	0.5- 2	F3d, F3e	Filled fissure, oriented parallel to main fault trend.
E3	DM2WW	utf, fis	U51?	U50	0.75	F3f	
E4	DM1EW	utf, dis,	U80	U70	2.5-3.5	F4a	Distributed zone of deformation
E4	DMIEW	dis, short, fold, thick	U75	U70	5.5-6.3	F4b	Distributed zone of deformation, folded sandy units and shortening and thickened tephra
E4	DM1EWext	utf, thick, short	U75	unkn	7.9, 9	F4c, F4d	Prominent shortened and thickened sand and tephra that appear to be subsequently faulted by E1

Table 1. (Continued)

E4	DM1WW	utf, dis	U75	U70	3-3.75	F4e	Distributed zone of deformation
E4	DM1WW	ang, fold	U75	U70	5.5	F4f	Angular unconformity. This area reveals a sandy and organic horizon that isn't seen anywhere else between U70 & U80.
E4	DM1WW	utf, fis	U75	U70	8.1	F4g	Expanded section? Minor faulting, correlates to minor faulting south of DM1EWext E1 broad deformation.
E4	DM2EW	dis, utf, fold	U75	U70	2.5-3.5	F4h	Both appear to be minor features Distributed deformation of faulted and folded sand
E4	DM2WW	dis, utf, fold	U75	U70	2-3.5	F4i	Distributed deformation of faulted and folded sand
E4	DM3EW	utf, vo	unkn	unkn	0.5-1	F4j	Faulted prominent organic horizon
E5	DM1	vo, thick	unkn	unkn	6.5-7.5	F5a	Event based on vertical offset of fluvial gravels that is overlain by no vertical offset in fine-grained sediments.
E6	DM3EW	utf, vo		Gravel	2-2.75	F6a	Appears to be capped by gravel.

Abbreviations: vo, vertical offset; utf, upward terminating fault; fis, fissure; dis, distributed deformation; short, horizontal shortening; fold, fold; thick, vertical thickening; ang, angular unconformity.

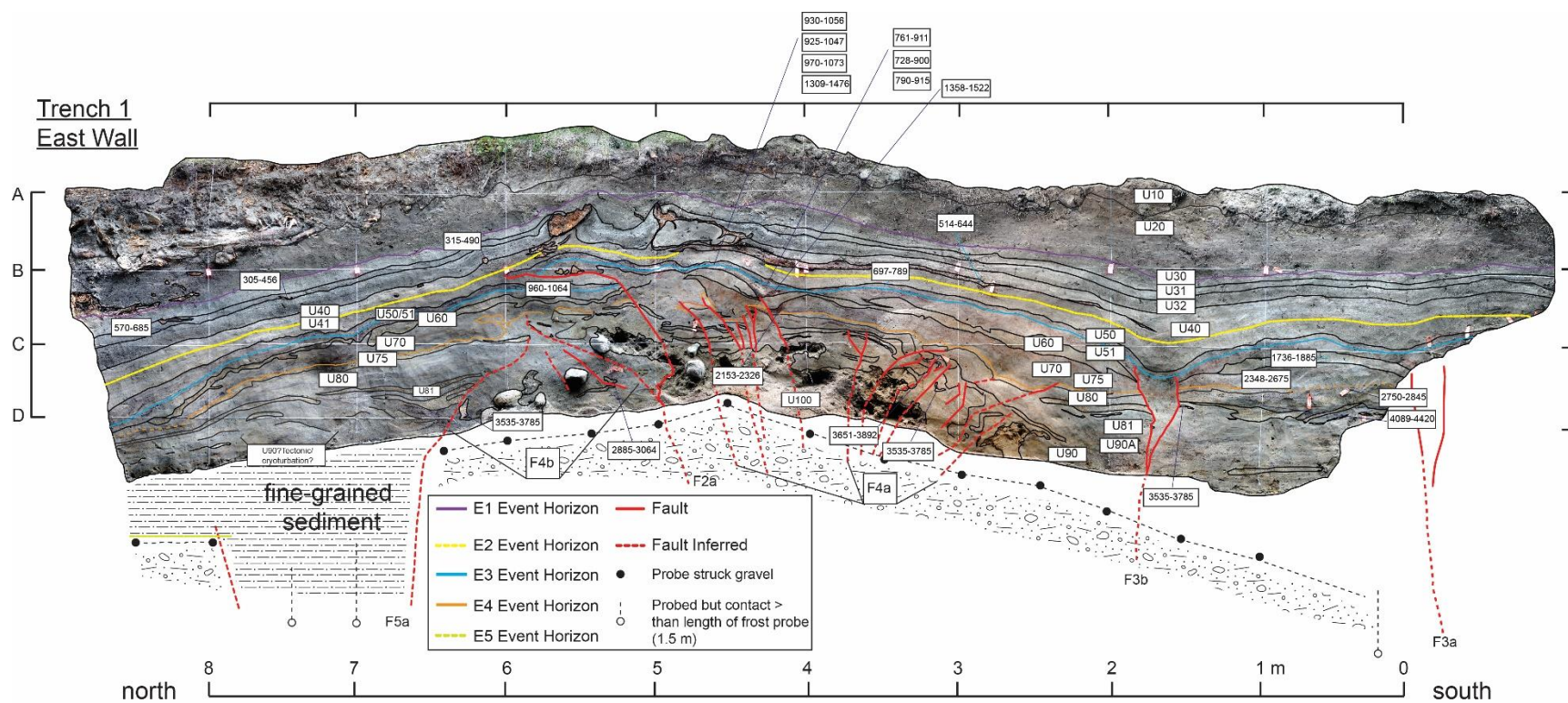


Figure 10. Dead Mouse trench one east wall.

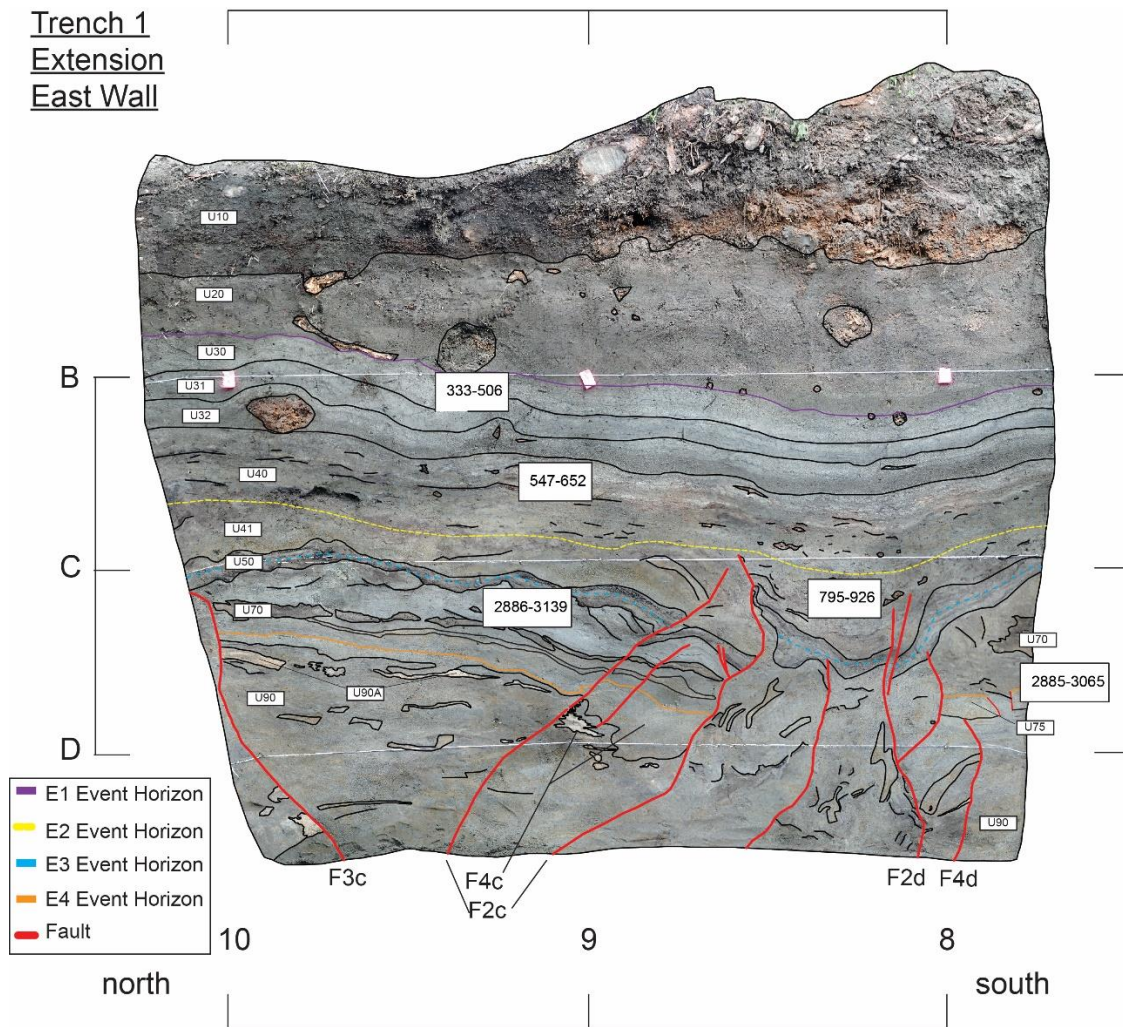


Figure 11. Dead Mouse trench one extension east wall.

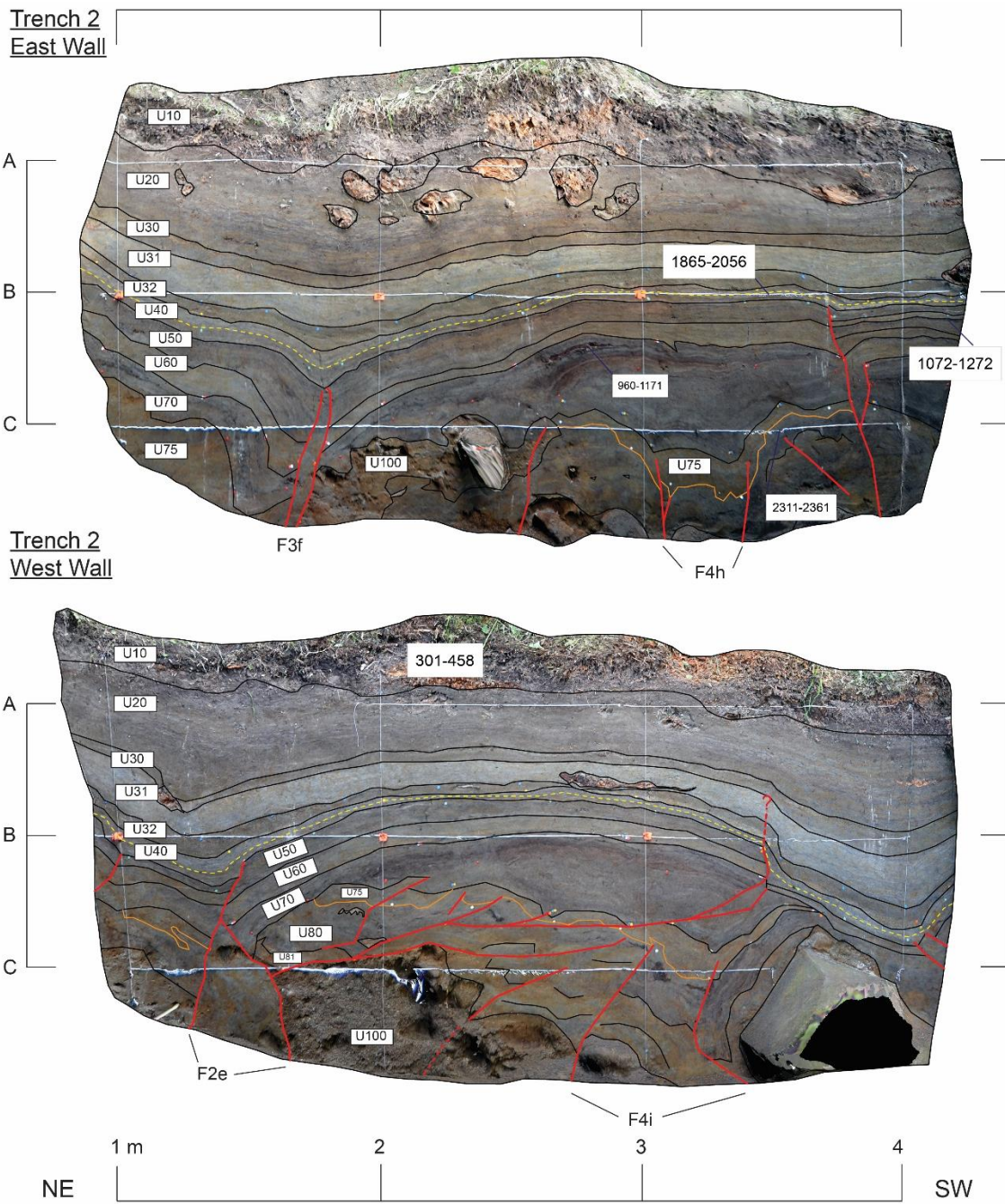


Figure 12. Dead Mouse trench two east and west walls.

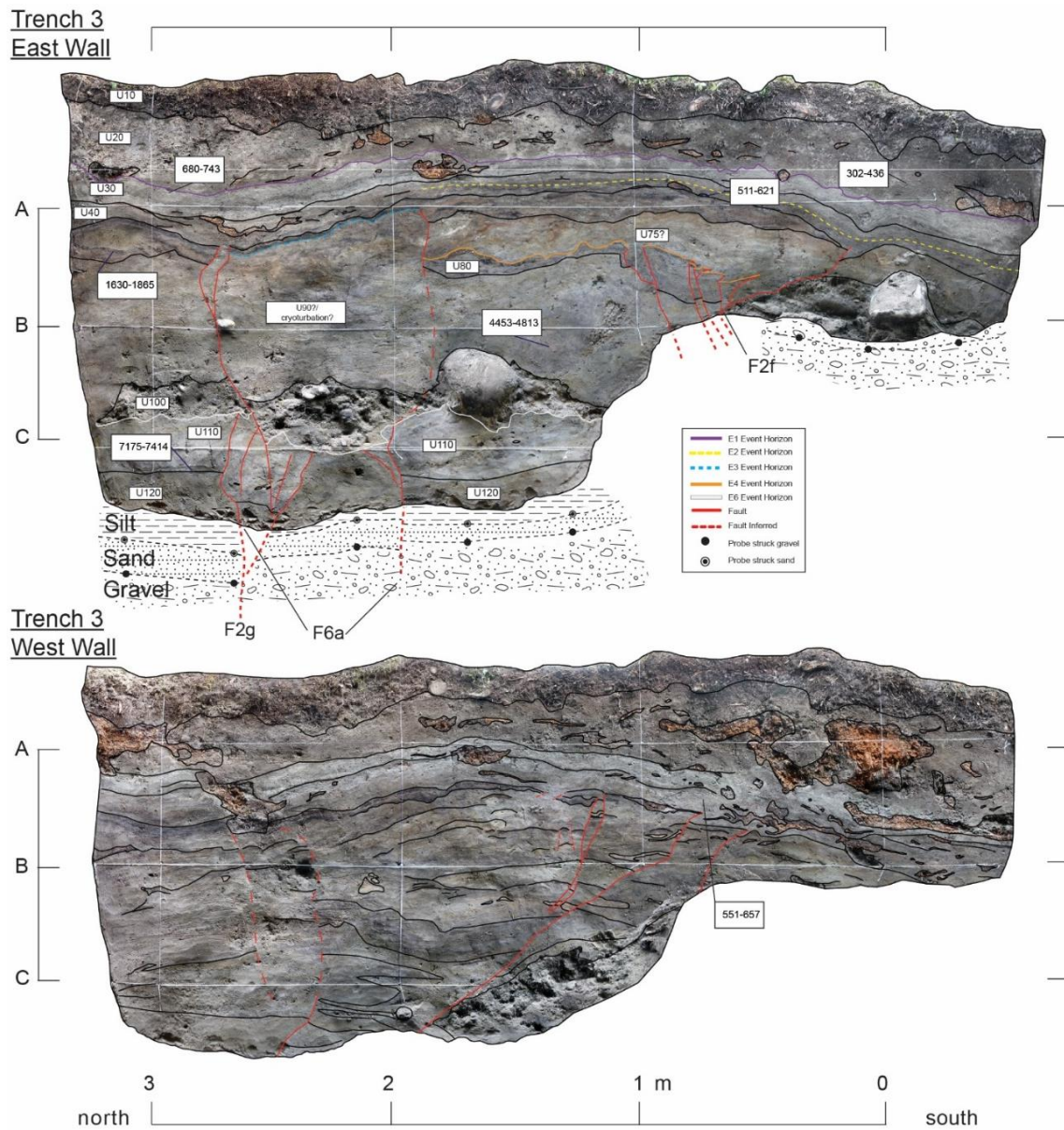


Figure 13. Dead Mouse trench three east and west walls. Note the high degree of bioturbation and lack of coherent stratigraphic units on the west wall.

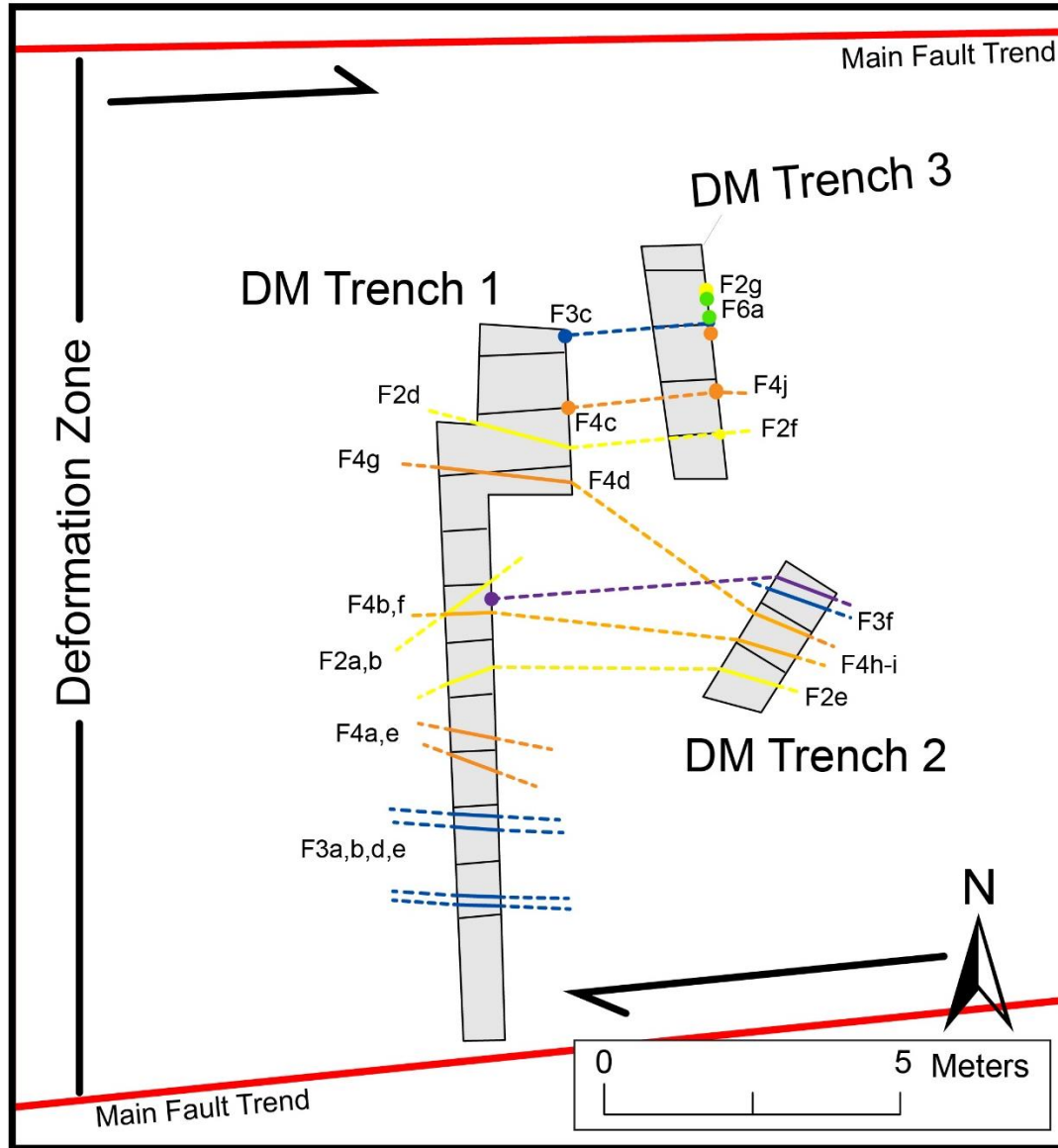


Figure 14. Trench locations with mapped distribution of event evidence. Black and gray outline trench boundary and black horizontal bars represent 1 m grid spacing. Purple- Event one (E1), Yellow- event two (E2), Blue- event three (E3), Orange- event four (E4), Green- event six (E6). Event five not represented. Red-width of geomorphic scarp and main trend of the Denali fault.

3.3 Earthquake Chronology

The relative sequence of earthquakes at the Dead Mouse site is well-defined through superposition of stratigraphic horizons and the cross-cutting relationships of faults and folds. We subdivide the stratigraphy into a framework of units to provide context for the description of superposition and chronological modeling. We use identifies units based on sedimentological differences to correlate strata from trench wall to trench wall and from trench to trench. To place stratigraphic horizons and earthquakes within an absolute age framework, we incorporated radiocarbon samples collected through the stratigraphic section and a tentatively correlated tephra into a stratigraphic age model. Using the Bayesian stratigraphic modeling approach we

employed OxCal 4.2.4 to calculate probability density functions for radiocarbon samples and event ages within the stratigraphy at the Dead Mouse site (Reimer et al., 2013; Lienkaemper and Bronk Ramsey, 2009; Bronk Ramsey, 2008 and 2009a). Mis-correlation of units between trenches would be the largest source of error in this relative sequence but due to the close proximity of the trenches and the sedimentologically distinct nature of the faulted horizons and sequences, the units appear to be well-correlated and internally consistent above U70 and exhibit greater variabilities below U70.

3.3.1 Radiocarbon Constraints

Organic-rich horizons are abundant at the Dead Mouse site and offer ample opportunity for stratigraphic age control, especially in the upper meter of stratigraphy. Sampled materials consisted of woody macrofossils, detrital charcoal, and in-situ charcoal (Figure 15) with individual cleaned and submitted sample masses varying between 9-339 mg. Each sample was examined under a binocular microscope to remove potential contaminants (excess sediment, root hairs, etc.) and we photographed and recorded corresponding sample characteristics. The majority of charcoal samples exhibited minimal weathering and appeared to be preserved in-situ or following minimal transport (Figure 15). However, a few samples were difficult to reliably differentiate between detrital or in-situ provenance. Our age chronology at the Dead Mouse site is constrained by 51 AMS radiocarbon analyses collected from a broad stratigraphic distribution in each of the three trenches (Table 2).

Radiocarbon analyses are consistent with previously discussed relative age constraints and the defined sequence of stratigraphic units. Nearly all sample ages increase with respect to increased depth within stratigraphic framework. We have however, excluded one sample age from U70 because the sample resulted in an age ~1700 years younger than the other eleven samples from the same unit (Table 2). Additionally, for the purpose of our sequence modeling we have grouped stratigraphic units U30, U31, U32, and U41 because there are no events within this interval, the units cover a relatively short period of time, and some of the sub units would otherwise produce inverted ages. Samples from these units include charcoal, leaves and woody material from roots. Roots were sampled from DM1 in 2012 with the interpretation that the tree had been killed during an earthquake, and because the roots penetrate below the ground surface, the age of the roots should be consistent with the overlying organic horizon. Fortunately the trees in the environment are characteristically shallow-rooted and unlikely to penetrate more than a few centimeters into the units below the organic surface layer at the time of growth. Sampling roots and organic material in undeformed stratigraphy directly above root penetration results in inverted ages. Grouping U30-41 as one phase maintains modeling consistency and has no effect on the age distribution of events.

Table 2. Radiocarbon samples and ages from Dead Mouse site.

Sample Name	Unit	¹⁴ C age (yr BP at 1σ)	Sample Type	δ ¹³ C	Age Cal BP	Trench	Wall	Lab ID
DFDM2WW 2A-M2	10	305 ± 25	w	-25.3	301-458	2	W	CAMS# 173716
DM3EW0.86,A5	20	305 ± 19	c	-24.0	302-436	3	E	D-AMS 013423
DM1EW7.5C31	30	312 ± 21	w	-24.4	305-456	1	E	D-AMS 013292
DM1extEW9.09,C46	30	393 ± 19	w	-27.4	333-506	1ext	E	D-AMS 013420
DM3EW1.68,A3	30-32	524 ± 22	w	-22.6	511-621	3	E	D-AMS 013287
DM1EW8.24,C18	31-32	705 ± 20	w	-22.6	570-685	1	E	D-AMS 013419
DM3EW3.9,A7	30-32	803 ± 20	w	-23.9	680-743	3	E	D-AMS 013424
SB-DFDM1-01	32	916 ± 27	w	-9.8		1	E	D-AMS 002085

DM1EW6.14,B7	32	349 ± 23	w	-19.0	315-490	1	E	D-AMS 013291
SB-DFDM1-02	32	882 ± 25	w	-30.7		1	E	D-AMS 002086
PTDM1-3	30-40	551 ± 36	c	-25	514-644	1	E	D-AMS 001361
DM1extEW8.88,C18	40	607 ± 22	w	-16.7	547-652	1ext	E	D-AMS 013289
PTDM1-1	41	937 ± 27	w	-20.0		1	E	D-AMS 001360
DM1extEW 8.18,D46	41	930 ± 25	w	-27.2	795-926	1ext	E	CAMS# 173707
DM1EW4.26,C42	40-50	871 ± 21	w	-23.9	728-900	1	E	D-AMS 013422
DM1EW4.55,B4D	40-50	905 ± 22	w	-23.3	761-911	1	E	D-AMS 013426
SB-DFDM1-5c	50	1186 ± 27	c	-24.9		1	E	D-AMS 002089
SB-DFDM1-5d	50	1174 ± 21	c	-28.7		1	E	D-AMS 002091
PTDM1-4	50	1110 ± 22	c	-26.9	964-1059	1	E	D-AMS 001362
DM1EW4.26,C37	50	926 ± 22	w	-19.1	790-915	1	E	D-AMS 013286
DM1EW3.60,B38	50	842 ± 22	w	-20.2	697-789	1	E	D-AMS 013290
DM1EW4.55,B4C	50	1052 ± 22	c	-23.2	925-1047	1	E	D-AMS 013294
DM1EW4.55B4B	50	1132 ± 19	c	-25	970-1073	1	E	D-AMS 013425
DM1EW 5.29,C40	50	1110 ± 25	c	-26.0	960-1064	1	E	CAMS# 173703
DM1EW 4.55,B4A	50	1075 ± 30	c	-25.4	930-1056	1	E	CAMS# 173708
DM1WW 4.72,C8	50	1155 ± 35	c	-25	979-1175	1	W	CAMS# 173712
SB-DFDM1-5a	51	1632 ± 25	w	-25		1	E	D-AMS 002090
DM1EW4.24,C32	51	1534 ± 23	w	-23.7	1358-1522	1	E	D-AMS 013285
DM1EW4.55,B4AW	51	1493 ± 27	w	-21.8	1309-1476	1	E	D-AMS 013293
DM1EW 0.66,C-6	60	1885 ± 25	w	-27.3	1736-1885	1	E	CAMS# 173702
DM3EW 4.18,B32	60	1825 ± 35	w	-26.8	1630-1865	3	E	CAMS# 173701
SB-DFDM1-13a	70	2859 ± 25	w	-27.2	2885-3064	1	E	D-AMS 002087
SB-DFDM1-10b	70	2674 ± 25	c	-27.7	2750-2845	1	E	D-AMS 002088
DM1EW4.19,C21	70	2221 ± 28	w	-17.6	2153-2326	1	E	D-AMS 013421
DM1EW 0.90,C-15	70	2395 ± 25	w	-26.8	2348-2675	1	E	CAMS# 173713
DM1extEW 7.8,D5	70	2860 ± 25	c	-25.0	2885-3065	1ext	E	CAMS# 173710
DM1extEW 9.15,D3	70	2875 ± 30	c	-26.6	2886-3139	1ext	E	CAMS# 173711
DM1WW 4.9,C5	70	2455 ± 25	w	-25.8	2365-2704	1	W	CAMS# 173704
DM1WW 5.44,D46	70	2395 ± 25	w	-25.5	2348-2670	1	W	CAMS# 173705
DM1extEW 7.8,D5	70	2860 ± 25	c	-25.0	2885-3065	1ext	E	CAMS# 173710
DM1extEW 9.15,D3	70?	2875 ± 30	c	-26.6	2886-3139	1ext	E	CAMS# 173711
DFDM2EW 14A-M3	70	2320 ± 25	c	-25.0	2311-2361	2	E	CAMS# 173718
DM3WW1.66,B25	70?	620 ± 25	w	-21.5	551-658	3	W	D-AMS 013288
DFDM1EW 10A-M3-01	80	3515 ± 40	w	-25	3651-3892	1	E	CAMS# 173715
DM1EW 1.20,C-35	80	3840 ± 60	w	-25	4089-4420	1	E	CAMS# 173706
DM3EW 2.36,C40	80	4100 ± 30	c	-23.8	4453-4813	3	E	CAMS# 173714
DM3EW 3.8,C-7	110	6345 ± 30	w	-28.1	7175-7414	3	E	CAMS# 173709
PTDM1-2	unkn	1080 ± 30	unkn	unkn	1013-1056	1	E	BL 333104
DFDM2EW 10A-M2	unkn	1125 ± 25	w	-24.8	960-1171	2	E	CAMS# 173717
DFDM2EW 8A-M4	unkn	1245 ± 35	w	-25	1072-1272	2	E	CAMS# 173719
DFDM2EW 6B-M3	unkn	1995 ± 40	w	-25	1865-2056	2	E	CAMS# 173720



Figure 15. View of charcoal sample under binocular microscope. This sample is one of the multiple charcoal samples at the Dead Mouse site where plant morphology and angular edges have been preserved. We suggest such morphology represents in-situ deposition and/or minimal transport.

3.3.2 Tephra

The presence of a volcanic tephra within the lowest half meter is persistent in trench one and recognizable in trench three. We have not analyzed the geochemistry, but the stratigraphic position and geographic location makes it potentially correlative with the ‘Hayes set H’ tephra Cantwell Ash or Hayes Tephra which have been identified in the region (Riehle et al., 1990; Wallace et al., 2014; Davies et al., 2016). If accurate, this classification constrains overlying sediments to <3910-4205 cal BP (Riehle et al., 1990; Wallace et al., 2014; Davies et al., 2016). The tephra is laterally discontinuous and occurs in ~1-5 cm thick tabular deposits that subsequently have been deformed resulting in ~1-10 cm long wavy horizons. Additionally, in several locations the tephra appears to be horizontally shortened and vertically thickened. Although the tephra tends to be laterally discontinuous, the stratigraphic position remains consistent throughout trench one, providing a unique marker horizon within the deeper stratigraphy where chronological constraints are limited.

3.3.3 Dead Mouse Earthquake Chronology

We calculate the probabilistic age ranges for each of the six interpreted events through the online statistical program OxCal 4.2.4 (Bronk Ramsey, 2008; 2009a). Modeling follows a Bayesian statistical approach to integrate a priori knowledge (stratigraphical units) and ages derived from analysis of radiocarbon and volcanic tephra (e.g., Bronk Ramsey, 2008). Modeling begins by attributing radiocarbon ages to individual stratigraphic units or phases. Then OxCal produces calibrated age probability density functions (PDF) for each radiocarbon sample and plots PDF’s within the framework of units previously constrained by relative age relationships. The utility of this age modeling approach comes from the ability to further constrain statistical ages by trimming overlapping tails of PDF’s when overlap occurs at any known unit boundary. At these locations PDF’s are trimmed and recalculated offering a more tightly constrained age distribution. In addition to modeling age distributions, OxCal produces PDF’s for each identified earthquake by bracketing the event age with overlying and underlying ages of units/phases.

The calibrated radiocarbon ages (cal BP) of our samples demonstrate a gradual increase in age from U10 to U60, whereas multiple age gaps occur for samples from U70-U120 (Figure 16). This age progression suggests approximately continuous sedimentation at the site without widespread erosion since ~2000 cal BP, and periods of erosion or long depositional hiatuses within the preceding stratigraphic record. The three most recent events occurred within the period of continuous sedimentation, which indicates that these three events likely represent the complete record of surface rupturing events for the Denali fault at the Dead Mouse site from the present day back to 1885 cal BP. Conversely, the oldest three events are less well-constrained and correspond with temporal gaps in our age control. Modeled event timing constrains events to the following 2-sigma age distribution: E1 to 440-316 cal yr BP, E2 to 835-740 cal yr BP, E3 to 1387-1126 cal yr BP, E4 to 3790-3020 cal yr BP, E5 to 5161-4531 cal yr BP and E6 to 7264-4943 cal yr BP (Table 3). Corresponding median event ages are 389, 786, 1259, 3406, 4745, and 6119 cal yr BP respectively.

Time intervals between earthquakes vary greatly for the earthquake chronology at this site. The two intervals defined by the most recent three earthquakes have similar durations, with modeled interval durations ranging from 325 to 612 years, and a median interval of 401 and 472 respectively (Table 4). The intervals between earthquakes E3 through E6 range from 155 to 2571 years with median intervals of 2148, 1369 and 1330 (Table 4). The post-E3 intervals are longer, either due to missing earthquakes during periods of erosion or non-deposition at the site and/or hiatuses in the occurrence of earthquakes on this portion of the fault. Variability in sedimentation and poor chronological constraints result in Boxcar-like probability density functions for E4 and E6 further complicating the last three recurrence intervals (Figure 16). Sedimentation is complicated for the lower section, but generally we see evidence for missing time due to erosion at the angular unconformity (Figure 9).

Table 3. Modeled event timing distribution and median age in calibrated years before present and calibrated AD/BC.

Event	Modeled cal BP		Median cal BP	Modeled cal AD/BC		Median cal AD/BC
	From	To		From	To	
E1	440	316	389	1511	1635	1562
E2	835	740	786	1115	1210	1164
E3	1387	1126	1259	563	825	692
E4	3790	3020	3406	1840	1071	1457
E5	5161	4531	4745	3206	2582	2796
E6	7264	4943	6119	5683	5230	5391

Table 4. Recurrence interval distribution and median duration in years.

Recurrence Interval	Years		Median Years
	From	To	
E1-E2	325	486	401
E2-E3	329	612	472
E3-E4	1722	2571	2148
E4-E5	838	1906	1369
E5-E6	155	2492	1330

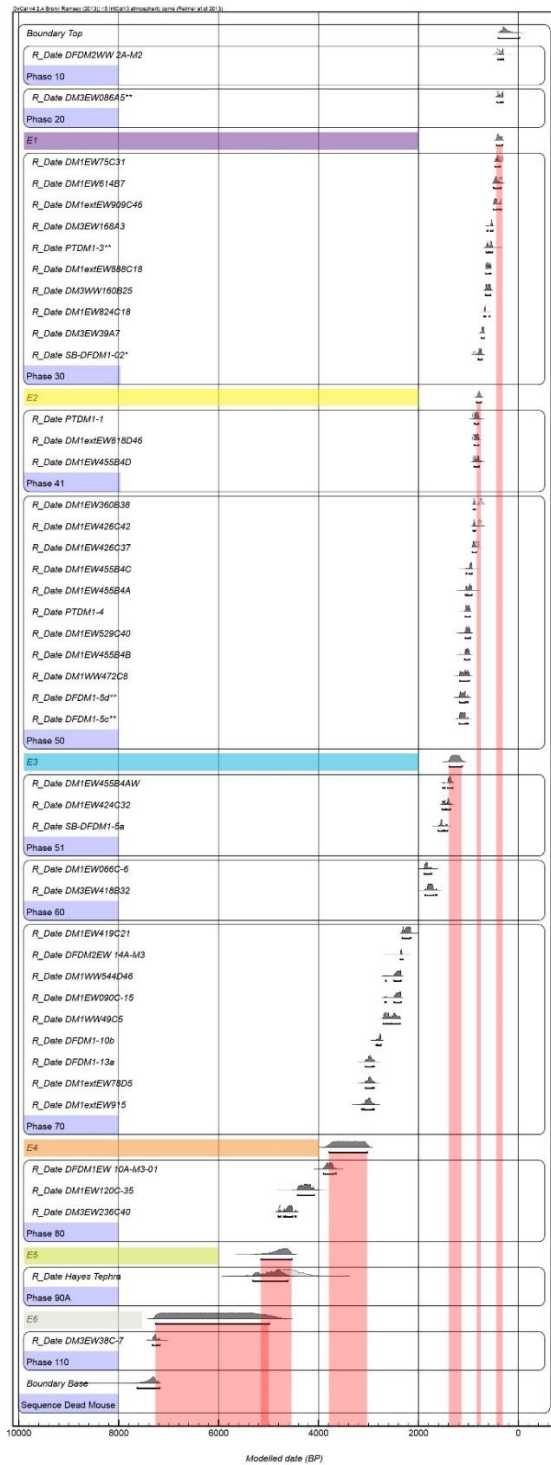


Figure 16. OxCal Model with probability density functions for radiocarbon dates. Sample age probabilities are plotted in stratigraphic order within previously described units (phase). The eleven phases represent the full depth of exposed sediments at the Dead Mouse site. Horizontal purple, yellow, blue, orange and green bars represent event horizons. Opaque vertical red bars highlight probability density age distribution for each of the six events.

4. Discussion

The lack of substantial temporal gaps within the past ~1800 years of stratigraphy suggests that our record for the past three earthquakes at the Dead Mouse site is complete. Beyond ~1800 cal BP the stratigraphy is punctuated by periods of erosion or non-deposition, and therefore the paleoearthquake record may be discontinuous (Figure 16). Comparing this record of earthquakes to other paleoearthquake sites along this portion of the Denali fault illustrates potential correlation of event timing at the Dead Mouse site, Schist Creek site, and the Delta River site (Figure 17). The most recent event at the Dead Mouse site correlates with timing and supports the most recent event Personius et al. (2015) infer from youthful fault geomorphology at the Schist Creek site (11 km east of Dead Mouse site). This event also correlates with event timing at the Delta River site (Plafker et al., 2006) and is consistent with the lichenometry-based age reported by Keskinen and Beget (2005) for an 8 km² landslide deposit that occurs ~4 km north of the Dead Mouse site. The timing of the penultimate event at the Dead Mouse site correlates to the penultimate event at the Rupture Fresh site, ~40 km to the west. At the rupture fresh site the penultimate event timing is ~1300 AD (D. Schwartz, personal communication, 2016). The ~100 yr age difference between sites could be due to differences in sampled organic materials, depositional environments and preservation. Timing for E3 at the Dead Mouse site also correlates to event timing at the Schist Creek site (Figure 17). The oldest three earthquakes recorded at the Dead Mouse site do not directly correspond with other known events along this section of the Denali fault but do overlap one poorly-constrained event at the Schist Creek site. Although the ages are not well-constrained, earthquakes E5 and E6 are the oldest earthquakes currently recognized on the entire Denali fault system. These events provide a foundation for correlation of potential future paleoearthquakes deeper in the stratigraphic history than what has already been documented.

Improvement upon the chronological record and event history at the Dead Mouse site relies upon additional dating methods, as well as potential expansion of trenching efforts. We collected a suite of samples for luminescence dating during summer 2015 and anticipate that future dating efforts with these samples will improve our chronological constraints for events E4, E5, and E6. These older events are bounded by units that suffer from the oxidation of much of the organic material, reducing the availability of material for radiocarbon dating. Additional chronological constraints from luminescence samples has the potential to change the modeled event age distribution and, in turn, provide fewer uncertainties on length of interseismic periods.

Our excavations did not reach undeformed stratigraphy on the north side of the Denali fault zone at the Dead Mouse site due to logistical constraints. However, based on distribution of deformation illustrated in high-resolution bare-earth topography and field observations, we suspect that undeformed stratigraphy outside the fault zone occurs less than 3 m north of our northernmost excavation extent. Based on the distributed nature of faulting from recent earthquakes through the site, we feel it is unlikely that a recent surface rupture would have occurred within this narrow distance without creating additional deformation that would have been captured by our excavations. However, we do recognize an arcuate surface depression extending from the terminus of a mapped surface *en echelon* rupture trace (Figure 4). This feature would require additional trenching to prove it has a non-tectonic origin, but we hypothesize that it is the result of frost wedging or the extension of an animal trail. Further expansion of DM3 to

the north would ensure we have captured the full width of deformation, but options for trench expansion are limited by permafrost and may be unproductive due to unclear stratigraphic relationships. For example, the middle to lower stratigraphic section in DM3 was difficult to reliably interpret due to apparent cryoturbation. Units 60 through U90 were undistinguishable in parts and a northward expansion is likely to expose similar stratigraphic convolution (Figure 13).

Surface topography at the Dead Mouse site reveals that it could be problematic to base historical event timing on geomorphic freshness of the scarp morphology. Surface topography at the Dead Mouse site appears to preserve evidence for scarp features relating to the penultimate event (F2d, F2a,b; Figure 14). At these locations, the surface geomorphology correlates to mapped subsurface structures dating back to 740-835 cal yr BP.

As a simple test for earthquake completeness at the Dead Mouse site, we plotted the earthquake age constraints at the Dead Mouse site against the cumulative displacement from characteristic 4 and 8 meter slip-per-event (Figure 18). We compare this slip accrual to the slip rate for the nearest slip rate site ~30 km to the west from Matmon et al. (2006). The minimum and maximum slip rates of 7.8 and 11 mm/yr on Figure 18 represent the full uncertainty for the Matmon et al. (2006) slip rate and provide the prediction for total strain accumulation over time. If we assume that earthquakes are slip-dependent and that they occur in response to a constant strain accumulation, then events plotted over time with cumulative slip will closely plot along the trendline of strain accumulation. These data reveal that for the Dead Mouse site paleoseismic history to be complete, it requires all of the events to be large, high displacement (~8 m) earthquakes and an average slip rate ≤ 7.8 mm/yr. Alternatively, if average slip-per-event is closer to 4 m, then our earthquake history is incomplete and would require a minimum of 4 additional events to fully release accumulated strain. Measurement of historical slip on the Denali fault of 4.5-8 m would suggest our modeled range is possible (Haeussler et al., 2004; Schwartz et al., 2003). However, we speculate that repeated slip of ≥ 8 m is unlikely. This is supported by a prehistoric slip-per event of ~4.2 m documented near the Dead Mouse site (D. Schwartz, personal communication, 2016) and the rare occurrence of displacements ≥ 8 m per events worldwide (Wells and Coppersmith, 1994). We suspect that our paleoearthquake record is missing several events between E3 and E4 and additional events between E4 and E5. Without better constraints on event timing for the latter three events or slip-per event it is difficult to reliably determine placement of missing events and recurrence. Our estimate of missing events is based on the two well-constrained recurrence intervals, the slope of strain release from the three most recent events, and supports the proposed recurrence rate of several hundred years by Schwartz and others (2012).

The infrastructural corridor adjacent to the Dead Mouse site has recently become the proposed site for a natural gas pipeline (Koehler et al., 2015). Data for event timing and earthquake behavior from our site provides necessary parameters to influence future seismic hazard mitigation. Given the geomorphic freshness of the fault scarp morphology, and our evidence for recurring large magnitude surface rupturing events we can assert that future events of similar magnitude and rupture morphology can be expected and should be considered in plans for future anthropogenic developments.

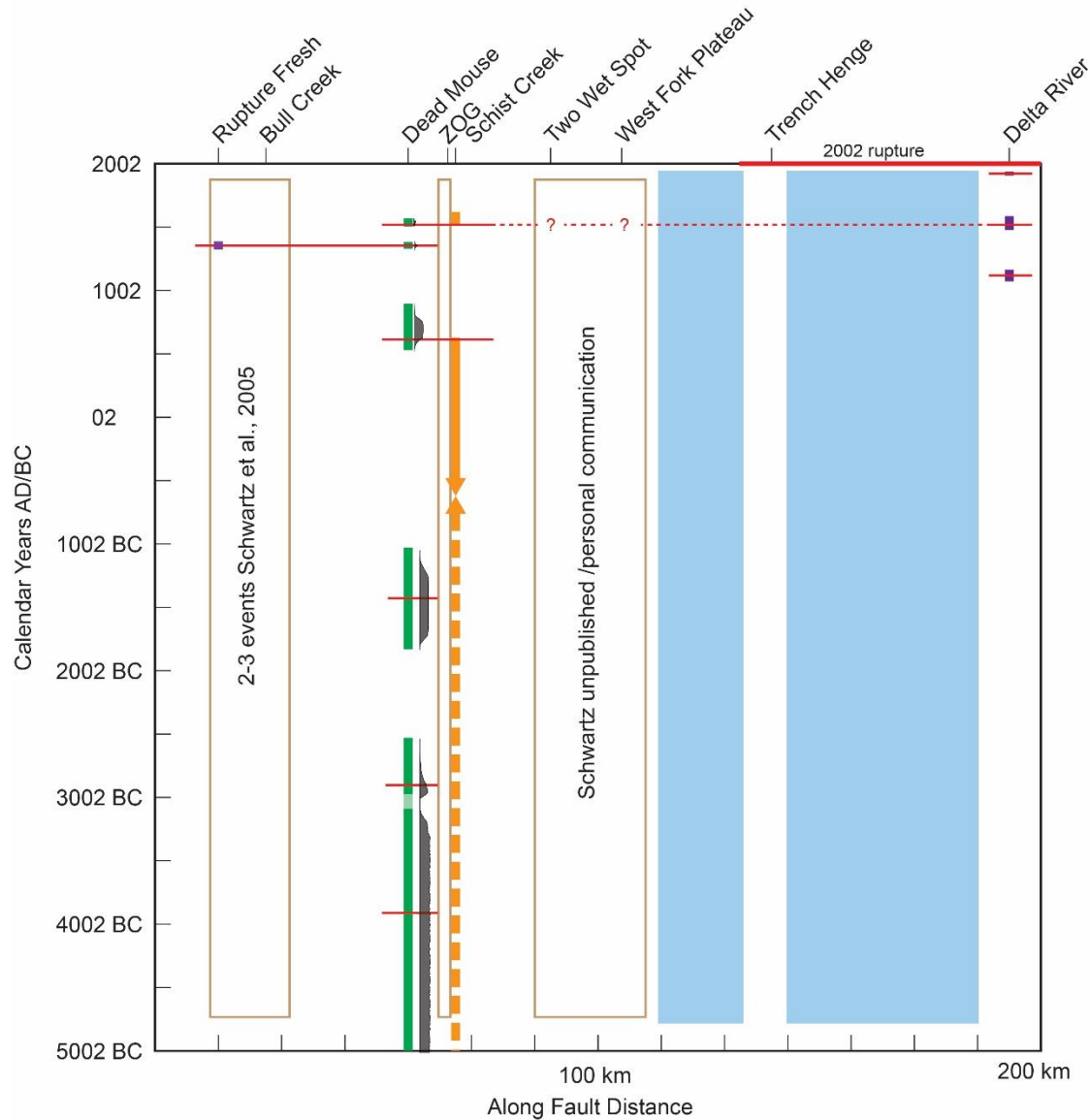


Figure 17. Along-fault distribution of paleoseismic sites for the west-central and central Denali fault. Similar event timing for event one and event two seen at the Schist Creek, as well as event one timing and the Delta River site event timing. Vertical green, orange and purple bars indicate distribution of event timing. Red horizontal bars indicated proposed event correlation and surface rupture for the 2002 M7.9 earthquake. Opposing orange arrows and dashed orange line represents two distinct events with lack of event bounding ages (Personius et al., 2015). Light-blue boxes show locations that are covered broadly by glaciers.

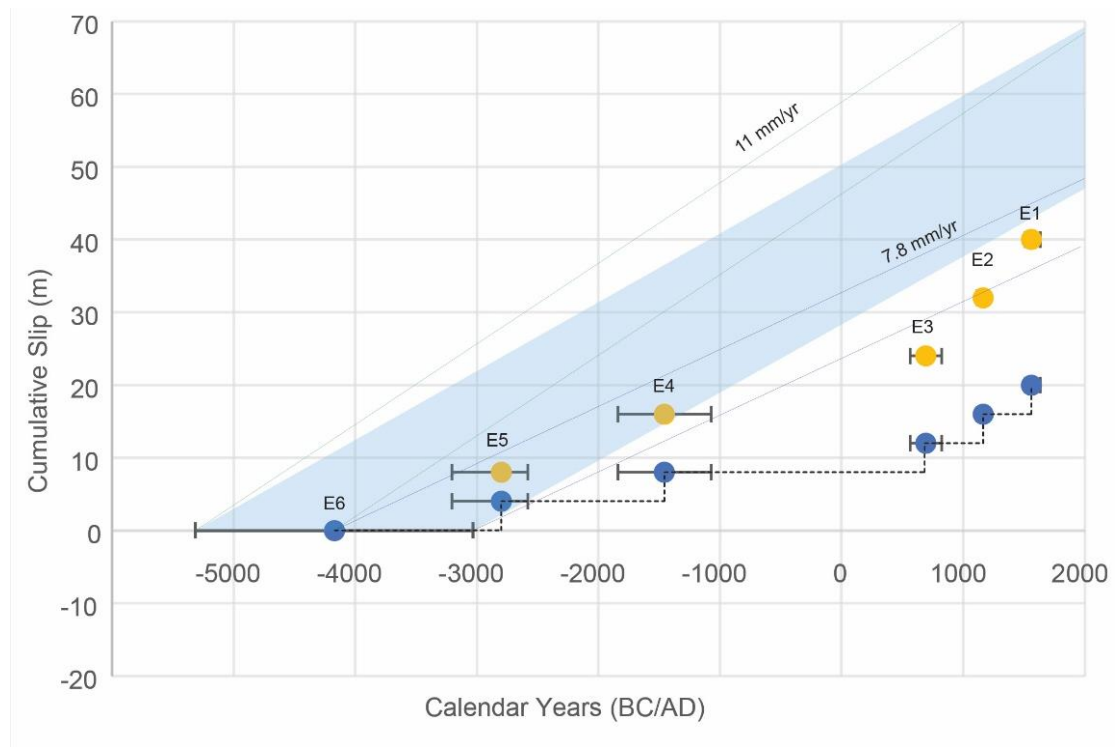


Figure 18. Earthquake timing plotted against proposed cumulative slip. Blue dots represent events with 4 m of slip-per-event. Yellow dots represent 8 m of slip-per-event. Trendlines plotted for strain accumulation of 11 and 7.8 mm/yr (Matmon et al., 2006).

Appendix A

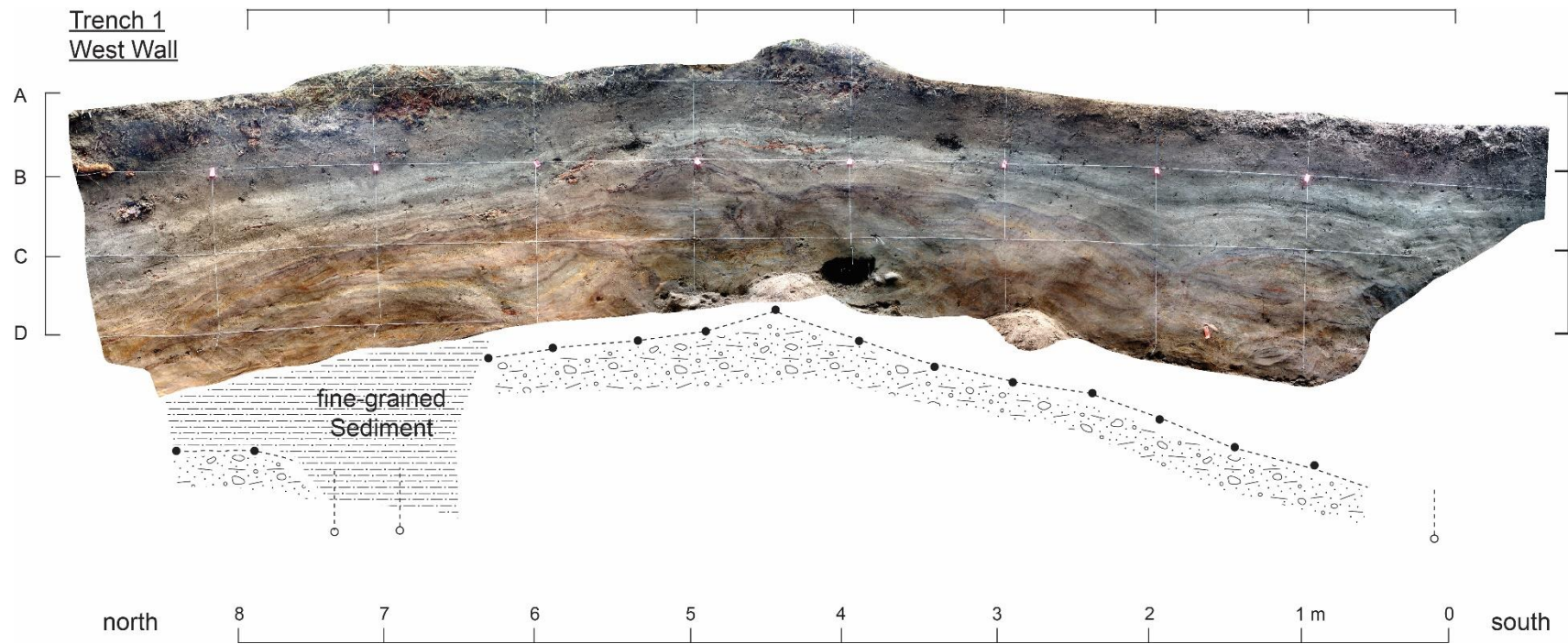


Figure 1. View of the west wall of Dead Mouse trench one without interpretations.

Appendix B

Table 1. Frost probe depth to gravel from trench floor surface.

Trench	Meter	Depth from trench floor to gravel contact (cm)	Sand depth (cm)	Notes
DM1	0.5	>probe		In fault zone and on ramp
	1	68		
	1.5	73	20	
	2	52	20	
	2.5	38	0	Start in sand/gravel
	3	37	na	Start in gravel
	3.5	49	0-49	
	4	26	0-26	
	4.5	8	0-8	
	5	25	0-25	
	5.5	29	0-29	
	6	24	variable	
	6.5	28	Variable	Sand occurrence highly variable depending upon probe placement
	7	>probe		Few cobbles dispersed but probe goes down nearly everywhere, frost jacking?
	7.5	>probe		
	8	83		
DM3	-0.2	7	0-7	
	0.2	12	0-12	
	0.5	17	0-17	
	1.25	34	24-34	Sand 10 cm thick
	1.75	30	15-30	Sand 15 cm thick
	2.25	28	8-28	Thickness change from previous 10 cm to 20cm
	2.75	41	24-41	Sand 17 cm thick
	3.1	52	38-52	Sand 14 cm thick

Table 2. Full list of radiocarbon and tephra samples. Directly copied from field notes and observations. Unit designation inaccurate.

Sample number (trench, wall, grid location)	Unit	Sample Type	Descriptive Location/Other
DM1EW 7.5,C31	30.2/30.3	Root	Slightly decomposed fibrous wood
DM1EW 8.24,C18	30.1/30.2	Root	Slightly decomposed fibrous wood, left side of sample within 30.1 and right side 30.2
DM1EW 8.44,D9	50	Bulk	Set of multiple organic horizons at the top of unit 50
DM1EW 7.88,C14	40	Bulk	Fine strings of organic horizons at the top of unit 40 just below the unit 30.3 contact
DM1EW 6.14,B7	30.3	Root	Slightly decomposed fibrous root at the base of 30.3
DM1EW 6.98,C8	50	Bulk	Most prominent organic horizon at the top of unit 50 ~ 6 cm down from base of unit 40
DM1EW 5.75,C38	50	Bulk	Lower horizon where unit 50 appears to splay in arcuate branch that terminates to the north. Possible location of fallen tree
DM1EW 5.55,B4	50	Bulk	Upper horizon of the arcuate splay of unit 50
DM1EW 5.6,B30	30.3	Wood	Thin fibrous wood that encircles sand
DM1EW 5.29,C40	50	Charcoal	Several pieces of detrital charcoal taken from single horizons. Located in upper horizon of the arcuate splay of unit 50. Same location as DM1EW 5.66,B8
DM1EW 4.53,C13	50A	Volcanic Ash	Light tan possible volcanic ash. This sample was extracted directly above sample DM1EW 4.62,C10
DM1EW 4.62,C10	50	Bulk	Bulk of arcuate apex up organic horizon. Collection of sample proved to be marginal due to a steep dip resulting in the majority of organic matter outside not captured.

DM1EW 4.57,B13	40	Root	Slightly decomposed fibrous wood and same location as 4T3-M2 from 2012 samples
DM1EW 3.64,C5	50A	Volcanic Ash	Light tan possible volcanic ash
DM1EW 4.51,B24	30.3	Wood	Slightly decomposed fibrous wood. Bark and woody core easily recognizable
DM1EW 4.26,C42	50	Bulk Horizon Scrape	Thin highly decomposed organic-rich horizon with discernable fibrous matrix. Taken from top horizon of minor colluvial wedge
DM1EW 4.26,C37	50	Bulk Horizon Scrape	Thin highly decomposed organic-rich horizon with discernable fibrous matrix. Taken from upper-middle horizon of minor colluvial wedge
DM1EW 4.24,C32	50	Bulk Horizon Scrape	Thin highly decomposed organic-rich horizon with discernable fibrous matrix. Taken from lower-middle horizon of minor colluvial wedge
DM1EW 4.19,C21	50	Bulk Horizon Scrape	Thin highly decomposed organic-rich horizon with discernable fibrous matrix. Taken from lowest horizon of minor colluvial wedge
DM1EW 4.55,B4	50	Bulk	Bulk sample from location where all organic-rich horizons from minor colluvial wedge feature appear to converge directly to the north.
DM1EW 1.85,C-9	50	Bulk	Large bulk sample at the top of unit 50. Organic-rich sag fill above important fault zone and appears to cap rupture
DM1EW 2.90,C24	50	Bulk Horizon Scrape	Thin organic-rich horizon. Sample at bottom of top of unit 50. Grades into sag to south
DM1EW 3.60,B38	50	Bulk Horizon Scrape	Thin organic-rich horizon. Sample at very top of 50. Caps event
DM1EW 3.60,B3800	50	Leaf	Matted leaf matter in 3mm horizon
DM1EW 1.20,C-35	Middle of 50	Bulk Horizon Scrape	Thin organic-rich horizon. Faulted by unit 50 event

DM1EW 0.90,C-15	Middle of 50	Bulk	Large bulk sample captures age of units prior to nearby rupture
DM1EW 0.66,C-6	Middle of 50	Horizon Scrape	Last organic horizon prior to event that located to the North on log. Sample consists of leaf litter
DM1WW 1.75,B36	30.1	Horizon Scrape	Short horizon scrape with sand and organics, most likely roots
DM1WW 2.28,B22	40	Bulk	Fine organic brown stringers located at the center of unit 40. Most likely sample quality is poor
DM1WW 1.40,C-3	50	Bulk Horizon Scrape	Dark horizon at the top of unit 50.
DM1WW 4.72,C8	50	Bulk Horizon Scrape	Black filled in fissure
DM1WW 4.9,C5	50	Bulk	Middle of unit 50 above event within 50
DM1WW 5.44,D46	50	Bulk Horizon Scrape	Faulted horizon fill
DM1extNW 10.2,C16	50	Charcoal	Top of unit 50, detrital?
DM1extEW 9.09,C46	30/20	Wood	Root at the unit 20-30 contact. Possibly deposited in situ
DM1extEW 8.88,C18	40	Bulk Horizon Scrape	Low content of roots and organics
DM1extEW 9.15,D35	50	Charcoal	Charcoal and wood within sand and faulted near the top of unit 50. Burn appears to be in situ
DM1extEW 8.85,D40	50	Charcoal	Pieces of charcoal. Fragments of thick burned wood along horizon
DM1extEW 8.18,D46	40/50	Bulk Horizon Scrape	Within unit 40/50 sag. Horizon is discontinuous within faulted zone
DM1extEW 7.8,D5	50	Bulk Horizon Scrape	Faulted organic horizon. Decomposed root?
DM3WW 1.66,B25	50?	Bulk	Taken from laminar root at top of the horizon. Appears to be near the top of unit 50 and next to the MRE
DM3WW 1.96,B33	30.3	Bulk	Organic material within dark sand near MRE

DM3WW 2.6,C3	50	Charcoal	Sample contains charcoal, dirt and sand. Near top of the gravel and charcoal in sandy lens
DM3WW 4.0,B11	50	Bulk	Collected from the uppermost section of unit 50. Sample contains leaf litter in thick organic horizon
DM3WW 4.4,B8	50	Bulk/Charcoal	Stratigraphically below the previous sample
DM3EW 3.8,C-7	50	Bulk	Thin organic-rich horizon below volcanic ash near the bottom of unit 50
DM3EW 1.66,B18	Middle of 50	Charcoal	In discontinuous disrupted soil horizon below top of 50
DM3EW3.9,A7	30.1	Bulk	Apparent leaf litter. Top of light colored sand and a potential cap for MRE
DM3EW 0.86,A5	20	Charcoal	Charcoal piece in sand, 9 cm above contact with unit 30
DM3EW 4.18,B32	50	Bulk	Organic-rich horizon at base of sand lens within the top of unit 50
DM3EW 2.36,C40	50	Charcoal	Charcoal piece in massive unit above gravels
DM3EW 1.68,A3	40	Bulk	Black sooty material in the middle of unit 40

Table 3. *OxCal modeling code*

Plot()

```
{
Sequence("Dead Mouse")
{
Boundary("Base");
Phase("110")
{
R_Date("DM3EW38C-7", 6345, 30);
};
Date("E6");
}
```

```

Phase("90A")
{
  R_Date("Hayes Tephra", 4120, 190);
};
Date("E5");
Phase("80")
{
  R_Date("DM3EW236C40", 4100, 30);
  R_Date("DM1EW120C-35", 3840, 60);
  R_Date("DFDM1EW 10A-M3-01", 3515, 40);
};
Date("E4");
Phase("70")
{
  R_Date("DM1extEW915", 2875, 30);
  R_Date("DM1extEW78D5", 2860, 25);
  R_Date("DFDM1-13a", 2859, 25);
  R_Date("DFDM1-10b", 2674, 25);
  R_Date("DM1WW49C5", 2455, 25);
  R_Date("DM1EW090C-15", 2395, 25);
  R_Date("DM1WW544D46", 2395, 25);
  R_Date("DFDM2EW 14A-M3", 2320, 25);
  R_Date("DM1EW419C21", 2221, 28);
};
Phase("60")
{
  R_Date("DM3EW418B32", 1825, 35);
  R_Date("DM1EW066C-6", 1885, 25);
};
Phase("51")
{
  R_Date("SB-DFDM1-5a", 1632, 25);
  R_Date("DM1EW424C32", 1534, 23);
  R_Date("DM1EW455B4AW", 1493, 27);
};
Date("E3");
Phase("50")
{
  R_Date("DFDM1-5c**", 1186, 27);
  R_Date("DFDM1-5d**", 1174, 21);
  R_Date("DM1WW472C8", 1155, 35);
  R_Date("DM1EW455B4B", 1132, 19);
  R_Date("DM1EW529C40", 1110, 25);
  R_Date("PTDM1-4", 1110, 22);
  R_Date("DM1EW455B4A", 1075, 30);
  R_Date("DM1EW455B4C", 1052, 22);
  R_Date("DM1EW426C37", 926, 22);
  R_Date("DM1EW426C42", 871, 21);
  R_Date("DM1EW360B38", 842, 22);
};
Phase("41")

```

```

{
  R_Date("DM1EW455B4D", 905, 22);
  R_Date("DM1extEW818D46", 930, 25);
  R_Date("PTDM1-1", 937, 27);
};
Date("E2");
Phase("30")
{
  R_Date("SB-DFDM1-02*", 882, 25);
  R_Date("DM3EW39A7", 803, 20);
  R_Date("DM1EW824C18", 705, 20);
  R_Date("DM3WW160B25", 620, 25);
  R_Date("DM1extEW888C18", 607, 22);
  R_Date("PTDM1-3**", 551, 36);
  R_Date("DM3EW168A3", 524, 22);
  R_Date("DM1extEW909C46", 363, 19);
  R_Date("DM1EW614B7", 349, 23);
  R_Date("DM1EW75C31", 312, 21);
};
Date("E1");
Phase("20")
{
  R_Date("DM3EW086A5**", 305, 19);
};
Phase("10")
{
  R_Date("DFDM2WW 2A-M2", 305, 25);
};
Boundary("Top");
};
Difference("E1-E2", "E1", "E2");
Difference("E2-E3", "E2", "E3");
Difference("E3-E4", "E3", "E4");
Difference("E4-E5", "E4", "E5");
Difference("E5-E6", "E5", "E6");
RI=(E1-E6)/5;
};

```

References

- Begét, J.E., Reger, R.D., Pinney, D.S., Gillispie, Tom, and Campbell, K.M., 1991, Correlation of the Holocene Jarvis Creek, Tangle Lakes, Cantwell, and Hayes tephras in south-central and central Alaska: *Quaternary Research*, v. 35, no. 2, p. 174–189.
- Bemis, S., Micklethwaite, S., Turner, D., James, M.R., Akciz, S., Thiele, S., and Bangash, H.A., 2014, Ground-based and UAV-Based photogrammetry: A multi-scale, high-resolution mapping tool for Structural Geology and Paleoseismology: *Journal of Structural Geology*, doi: 10.1016/j.jsg.2014.10.007.
- Bemis, S.P., Weldon, R.J., and Carver, G.A., 2015, Slip partitioning along a continuously curved fault: Quaternary geologic controls on Denali fault system slip partitioning, growth of the Alaska Range, and the tectonics of south-central Alaska: *Lithosphere*, p. L352.1, doi: 10.1130/L352.1.
- Bowers, P., 1979, The Cantwell ash bed, a Holocene tephra in the central Alaska Range, Alaska Division of Geological and Geophysical Surveys Geologic Report 61, 19-24.
- Briner, J.P., and Kaufman, D.S., 2008, Late Pleistocene mountain glaciation in Alaska: key chronologies: *Journal of Quaternary Science*, v. 23, p. 659–670, doi: 10.1002/jqs.1196.
- Bronk Ramsey, C., 2008, Deposition models for chronological records. *Quaternary Science Reviews*, 27(1-2), 42-60.
- Bronk Ramsey, C., 2009a, Bayesian analysis of radiocarbon dates. *Radiocarbon*, 51(1), 337-360.
- Carver, G.A., Plafker, G., Metz, M.C., Cluff, L., Slemmons, B., Johnson, E., Roddick, J., and Sorensen, S., 2004, Surface rupture on the Denali fault interpreted from tree damage during the 1912 Delta River Mw 7.2–7.4 earthquake—Implications for the 2004 Denali fault earthquake slip distribution: *Bulletin of the Seismological Society of America*, v. 94, no. 6B, p. S58–S71.
- Wells, D. L., and Coppersmith, K. J., 1994, New Empirical Relationships among Magnitude, Rupture Length, Rupture Width, Rupture Area, and Surface Displacement, *Bulletin of the Seismological Society of America*, Vol. 84, No. 4 pp. 974-1002.
- Csejtey, B., Mullen, M.W., Cox, D.P., and Stricker, G.D., 1992, Geology and geochronology of the Healy Quadrangle, south-central Alaska: U.S. Geological Survey Miscellaneous Investigations 1191, 63 p., 1 sheet, 1:250,000 scale.
- Dortch, J.M., Owen, L.A., Caffee, M.W., LI, D., Lowell, T.V., 2010. Beryllium-10 surface exposure dating of glacial successions in the Central Alaska Range, *Journal of Quaternary Science* 25, 1259-1269.
- Eberhart-Phillips, D., Haeussler, P.J., Freymueller, J.T., Frankel, A.D., Rubin, C.M., Craw, P., Ratchkovski, N.A., Anderson, G., Carver, G.A., Crone, A.J., Dawson, T.E., Fletcher, H., Hansen, R., Harp, E.L., et al., 2003, The 2002 Denali fault Earthquake, Alaska: A Large Magnitude, Slip-Partitioned Event: *Science*, v. 300, p. 1113–1119
- Haeussler, P.J., 2009, Surface rupture map of the 2002 M7.9 Denali fault earthquake, Alaska: digital data: U.S. Geological Survey Data Series DS-0422, 9, 1 sheet p.

- Eberhart-Phillips, D., Christensen, D.H., Brocher, T.M., Hansen, R., Ruppert, N.A., Haeussler, P.J., and Abers, G.A., 2006, Imaging the transition from Aleutian subduction to Yakutat collision in Central Alaska, with local earthquakes and active source data: *Journal of Geophysical Research*, v. 111, p. B11303, doi: 10.1029/2005JB004240.
- Freymueller, J.T., Woodard, H., Cohen, S.C., Cross, R., Elliott, J., Larsen, C.F., Hreinsdóttir, S., and Zweck, C., 2008, Active Deformation Processes in Alaska, Based on 15 years of GPS measurements, in Freymueller, J.T., Haeussler, P.J., Wesson, R., and Ekström, G., eds., *Active Tectonics and Seismic Potential of Alaska*: Washington, D.C., American Geophysical Union Geophysical Monograph Series 179, p. 1–42.
- Grantz, A., 1966, Strike-slip faults in Alaska: U.S. Geological Survey Open-File Report 267, 82 p.
- Haeussler, P.J., Schwartz, D.P., Dawson, T.E., Stenner, H.D., Lienkaemper, J.J., Sherrod, Brian, Cinti, F.R., Montone, Paola, Craw, P.A., Crone, A.J., and Personius, S.F., 2004, Surface rupture and slip distribution of the Denali and Totschunda faults in the 3 November 2002 M7.9 earthquake, Alaska: *Bulletin of the Seismological Society of America*, v. 94, no. 6B, p. S23–S52.
- Haeussler, P.J., 2008, An Overview of the Neotectonics of Interior Alaska: Far-Field Deformation From the Yakutat Microplate Collision, in Freymueller, J.T., Haeussler, P.J., Wesson, R.L., and Ekström, G. eds., *Active Tectonics and Seismic Potential of Alaska*, American Geophysical Union Geophysical Monograph Series 179, American Geophysical Union, Washington, D.C., p. 83–108.
- Haeussler, P.J., Matmon, A., Schwartz, D.P., Seitz, G., Crone, A.J., 2012, The Denali fault and Interior Alaska Tectonics in Mid- to Late-Cenozoic Time: American Geophysical Union, Fall Meeting 2012, abstract#T14A-04
- Hamilton, T.D., 1994, Late Cenozoic glaciation of Alaska, in Plafker, G. and Berg, H.C. eds., *The Geology of Alaska*, G-1, Boulder, Colorado, Geological Society of America, *Geology of North America*, v. G-1, p. 813–844.
- Hickman, R. G., Sherwood, K. W., and Cradock, C., 1990, Structural evolution of the early Tertiary Cantwell basin, south-central Alaska: *Tectonics*, v. 9, p. 365–369.
- Hubbard, T.D., Koehler, R.D., and Combellick, R.A., 2011, High-resolution lidar data for Alaska infrastructure corridors, in GGS Staff, *Elevation Datasets of Alaska*: Alaska Division of Geological & Geophysical Surveys Raw Data File 2011-3, 291 p. doi:10.14509/22722
- Keskinen, M., and Beget, J., 2005, Age of most Recent Motion on the Western Denali fault from Lichenometric Dating of a Large Rockfall Avalanche and Offset Moraines, in *Eos Transactions*.
- Koehler, R.D., Personius, S.F., Schwartz, D.P., Haeussler, P.J., and Seitz, G.G., 2011, A Paleoseismic study along the central Denali fault, Chistochina Glacier area, south-central Alaska, Division of Geological & Geophysical Surveys report of investigation, p. 1–17.
- Lienkaemper, J. J., and Bronk Ramsey, C., 2009, OxCal: Versatile Tool for Developing Paleoearthquake Chronologies—A Primer. *Seismological Research Letters*. V. 80(3) p.431–434.

- Matmon, A., Schwartz, D.P., Haeussler, P.J., Finkel, R., Lienkaemper, J.J., Stenner, H.D., and Dawson, T., 2006, Denali fault slip rates and Holocene-late Pleistocene kinematics of central Alaska: *Geology*, v. 34, p. 645–648, doi: 10.1130/G22361.1.
- Mériaux, A.-S., Sieh, K., Finkel, R.C., Rubin, C.M., Taylor, M.H., Meltzner, A.J., and Ryerson, F.J., 2009, Kinematic behavior of southern Alaska constrained by westward decreasing postglacial slip rates on the Denali fault, Alaska: *Journal of Geophysical Research*, v. 114, p. B03404, doi:10.1029/2007JB005053.
- Miller, M. L., Bradley, D. C., Bundtzen, T. K., and McClelland, W., 2002, Late Cretaceous through Cenozoic Strike-Slip Tectonics of Southwestern Alaska, *The Journal of Geology*, Vol. 110(3), p.247.
- Nokleberg, W. J., Jones, D. L., and Silberling, N. J., 1985, Origin and tectonic evolution of the Maclaren and Wrangellia terranes, eastern Alaska Range, Alaska: *Geological Society of America Bulletin*, V. 96, p.1251-1270.
- Personius, S.F., Crone, A.J., Burns, P.A.C, and Rozell, Ned, 2015, Paleoseismology of the Denali fault system at the Schist Creek site, central Alaska: U.S. Geological Survey Open-File Report 2015-1225, 15 p., 1 oversize plate, <http://dx.doi.org/10.3133/ofr20151225>.
- Plafker, George, Carver, G.A., Cluff, Lloyd, and Metz, Mike, 2006, Historic and paleo-seismic evidence for non-characteristic earthquakes and the seismic cycle at the Delta River crossing of the Denali fault, Alaska [abs.]: 102nd Annual Meeting of the Cordilleran Section, Geological Society of America, May 8–10, Anchorage, Alaska, v. 38, 96 p.
- Plafker, George, and Berg, H.C., 1994, Review of the geology and tectonic evolution of Alaska, in Plafker, George, and Berg, H.C., eds., *The Geology of Alaska*: Boulder, Colorado, Geological Society of America, *The Geology of North America*, v. G-1, p. 989–1,021.
- Reimer, P. J., Bard, E., Bayliss, A., Beck, J. W., Blackwell, P. G., Bronk Ramsey, C., Grootes, P. M., Guilderson, T. P., Hafliðason, H., Hajdas, I., Hatt, C., Heaton, T. J., Hoffmann, D. L., Hogg, A. G., Hughen, K. A., Kaiser, K. F., Kromer, B., Manning, S. W., Niu, M., Reimer, R. W., Richards, D. A., Scott, E. M., Southon, J. R., Staff, R. A., Turney, C. S. M., & van der Plicht, J., 2013, IntCal13 and Marine13 Radiocarbon Age Calibration Curves 0-50,000 Years cal BP. *Radiocarbon*, 55(4).
- Reitman, N.G., Scott, Bennett, S.E.K., Gold, R.D., Briggs, R.W., and DuRoss, C.B., 2015, High-Resolution Trench Photomosaics from Image-Based Modeling: Workflow and Error Analysis, *Bulletin of the Seismological Society of America*, Vol. 105, No. 5, doi: 10.1785/0120150041.
- Ridgway, K.D., Trop, J.M., Nokleberg, W.J., Davidson, C.M., Eastham, K.R., 2002, Mesozoic and Cenozoic tectonics of the eastern and central Alaska Range: Progressive basin development and deformation in a suture zone, *GSA Bulletin*; December 2002; v. 114; no. 12; p. 1480–1504, doi: 10.1130/0016-7606(2002)114<1480:MACTOT>2.0.CO;2
- Ridgway, K.D., Thoms, E.E., Layer, Paul W., Lesh, M.E., White, J.M., and Smith, S.V., 2007, Neogene transpressional foreland basin development on the north side of the central Alaska Range, Usibelli Group and Nenana Gravel, Tanana basin, in Ridgway, K.D., Trop, J.M., Glen, J.M.G., and O'Neill, J.M., eds., *Tectonic Growth of a Collisional Continental Margin: Crustal Evolution of Southern Alaska*: Geological Society of America Special Paper 431, p. 507–547.

Riehle, J.R., Bowers, P.M., and Ager, T.A., 1990, The Hayes tephra deposits, an upper Holocene marker horizon in south-central Alaska, *Quaternary Research* 33, 276-290.

Schwartz, D.P., and the Denali fault earthquake geology working group, 2003, Paleo-earthquakes on the Denali–Totschunda fault system—Preliminary observations of slip and timing: American Geophysical Union, fall meeting, abstract # S11B-03.

Schwartz, D.P., Haeussler, P.J., Seitz, G.G., Dawson, T.E., Stenner, H.D., Matmon, A., Crone A.J., Personius, S.F., Burns, P.B., Cadena, A., and Thoms, E., 2005, Unraveling the earthquake history of the Denali fault system, Alaska—Filling a blank canvas with paleoearthquakes [abs.]: *Eos Transactions, American Geophysical Union*, v. 86, no. 52, Fall Meeting Supplement, abstract U42A-06.

Schwartz, D.P., Haeussler, P.J., Seitz, G.G., and Dawson, T.E., 2012, Why the 2002 Denali fault rupture propagated onto the Totschunda fault: Implications for fault branching and seismic hazards: *Journal of Geophysical Research: Solid Earth*, v. 117, p. n/a–n/a, doi: 10.1029/2011JB008918.

Schwartz, D.P., Haeussler, P.J., Seitz, G.G., Koehler, R.D., Personius, S.F., Crone, A.J., and Dawson, T.E., 2014, Recurrence of large earthquakes along the Denali fault system [abs.]: *Seismological Society of America Annual Meeting, Seismological Research Letters*, v. 85, no. 2, p. 474.

Seitz, G.G., Haeussler, P.J., Crone, A.J., Lipovsky, Panya, and Schwartz, D.P., 2008, Eastern Denali fault slip rate and paleoseismic history, Kluane Lake area, Yukon Territory, Canada [abs.]: *Eos Transactions American Geophysical Union*, v. 89, no. 53, Fall Meeting Supplement, abstract T53B-1947.

Sherwood, K.W., and Craddock, Campbell, 1979, General geology of the central Alaska Range between the Nenana River and Mount Deborah: Alaska Division of Geological and Geophysical Surveys Open File Report 116, 22 p., 3 plates, scale 1:63,360.

Thoms, E.E., 2000, Late Cenozoic unroofing sequence and foreland basin development of the central Alaska Range: Implications from the Nenana Gravel [M.S. thesis]: University of Alaska Fairbanks, 221 p.

Wesson, R.L., Boyd, O.S., Mueller, C.S., Bufe, C.G., Frankel, A.D., and Petersen, M.D., 2007, Revision of time-independent probabilistic seismic hazard maps for Alaska: U.S. Geological Survey Open-File Report 2007-1043

